

Technical paper

Robotic disc grinding path planning method based on multi-objective optimization for nuclear reactor coolant pump casing

Bo Zhou^{a,b,*}, Tongtong Tian^{a,b}

^a Shenyang Institute of Automation, Chinese Academy of Sciences, Shenyang 110169, China

^b Institutes for Robotics and Intelligent Manufacturing, Chinese Academy of Sciences, Shenyang 110169, China

ARTICLE INFO

Keywords:

Multi-objective optimization

Inverse kinematics

Path planning

ABSTRACT

In the nuclear industry, the finishing grinding work of the nuclear reactor coolant pump (RCP) casing is mainly performed manually. Uncontrollable grinding tasks cause the grinding disc to be easily worn during the grinding process, which will greatly affect the grinding accuracy and efficiency. This paper introduces a path planning method that can efficiently and accurately perform a disc grinding task on an RCP casing. First, we provide a wear model for rigid grinding discs and verify its accuracy through finite element simulations and experiments. It can be used to predict the wear conditions of grinding discs during grinding. Then, a series of linear geodesic offset paths with the shortest path length characteristic can be generated and converted to NURBS interpolation paths. The velocity, acceleration, and jerk of the of the NURBS interpolated path generated by the S-shaped acceleration/deceleration (ACC/DEC) feedrate planning method in Cartesian space can be converted into the corresponding angular velocity, acceleration, and jerk of each joint in joint space to ensure that the grinding tasks can be performed under appropriate kinematic constraints; Then, an improved NSGA-II algorithm is proposed and its performance is verified based on benchmark test problem suite in three indicators. The verification results showed that the solution set generated by the proposed algorithm has good distribution uniformity, is closer to the true boundary, and has good convergence compared with other advanced optimization algorithms; Furthermore, by substituting the multi-objective optimization functions and kinematic constraints into the improved NSGA-II algorithm, the compromise minimization problem of grinding time, impact, and disc wear can be solved. The simulation and experimental results demonstrate the superiority and effectiveness of the optimized geodesic grinding paths in terms of grinding precision, accuracy, stability, and efficiency. In contrast, multi-directional paths, e.g., optimized cycloid paths, will produce varying grinding contact forces and varying disc sliding velocities, which will lead to more complex material removal situations, thus affecting the accuracy of the optimization solution.

1. Introduction

As one of the most important components, the RCP is located at the heart of the nuclear island and needs to be built with the same service life (60 years) as a typical third-generation nuclear power plant. Although it has large external dimensions, its manufacturing accuracy will affect the overall assembly accuracy of the nuclear island because it is located inside the containment and connected with other components. Therefore, its casing requires finish grinding to meet the manufacturing accuracy requirements. Usually, the milling process before grinding can be performed by a large computerized numerical control (CNC) system. However, considering the complex geometry of the RCP casing, the

inherent processing scope of the equipment, and the processing cost, the grinding system (equipped with grinding tools) modified from the traditional CNC system is not suitable for grinding RCP casings. Due to the inherent high mechanical strength of the RCP casing and the manufacturing requirements of removing the significant residual scallop height in the grinding stage, it is more effective and economical to use a grinding disc that is more similar to a rigid disc, because it can withstand a greater grinding force and achieve a higher metal removal rate. This will cause problems in the wear and replacement of grinding discs, but there has been no systematic research on the disc wear model and high-quality grinding path of heavy-duty robots. At present, manual disc grinding (the disc contacts the workpiece surface at a small angle, which

* Corresponding author at: Shenyang Institute of Automation, Chinese Academy of Sciences, Shenyang 110169, China.

E-mail address: zhoubo@sia.cn (B. Zhou).

<https://doi.org/10.1016/j.jmansys.2024.10.021>

Received 4 July 2024; Received in revised form 11 August 2024; Accepted 23 October 2024

Available online 1 November 2024

0278-6125/© 2024 The Society of Manufacturing Engineers. Published by Elsevier Ltd. All rights are reserved, including those for text and data mining, AI training, and similar technologies.

usually ranges from 5° to 25°) is still widely used in the precision grinding stage of RCP casings. This small angle can prevent the speed of the disc center from being zero and prevent the accumulation of abrasive dust [1]. The disc grinding method can be used to remove redundant materials from work pieces with complex shapes, e.g., weld beads [2]. The disc grinding work of RCP casings has not yet been robotized, and manual work will inevitably lead to either low efficiency or inconsistent quality. In particular, the harsh environment in the grinding process has inherent safety risks and can lead to pneumoconiosis among workers [3]. Industrial robots (manipulator type) with relatively large manufacturing scopes and low costs are designed to release humans from repetitive tasks (i.e., grinding, measuring, and electric welding). They are the preferred tools for many aerospace and automobile manufacturing industries [4]. Some prototype robot systems developed for special applications where industrial robots cannot be used have been used to grind large mechanical components [5], e.g., wind turbine blades, high speed rail bodies, and new energy bus bodies, but almost no empirical research on the automatic manufacturing of RCP casings has been carried out. Compared with those of industrial robots, the development cost of prototype robot systems is high, the development cycle is long, and their function is difficult to expand. Both industrial robots and prototype robotic systems must be programmed, e.g., integrated with offline programming functions, to perform their tasks [6]. However, these existing offline programming softwares cannot meet the needs of high-efficiency and high-quality grinding of RCP castings.

In this work, we developed and verified a new smooth path planning method to realize disc grinding work on RCP casings. First, we generate two paths with excellent characteristics in terms of grinding path length and multi-directionality on the reconstructed mesh via graphics calculation methods, and convert them into corresponding higher-order end effector motion parametric curves, i.e., NURBS interpolation paths, so that the grinding motion of the robot is stable and continuous. Then, according to the inverse kinematics solution, the angular motion curve $\theta(t) = [\theta_1(t), \theta_2(t), \dots, \theta_6(t)]$ and the relevant dynamic characteristic curve of each joint can be calculated; then, these angular motion parameters can be optimized by implementing a multi-objective optimization algorithm to solve the compromise minimization problem of grinding time (f_1), impact (f_2), and disc wear (f_3). The path planning procedures are shown in Fig. 1.

2. Related research work

2.1. Disc wear

Due to the excellent mechanical properties of stainless steel, disc wear is extremely severe during the grinding process of RCP casings. Moreover, stainless steel exhibits strong chemical affinity under high temperature and pressure, allowing the generated abrasives to easily adhere to the abrasive particles and block the gaps between them, resulting in the loss of grinding ability of the grinding disc [7]. Under these combined actions, the contact area between the grinding disc and the workpiece increases, leading to a rapid increase in the generation of grinding heat, which prevents the heat from being quickly transferred and can easily cause grinding burns on the RCP. Therefore, the wear of the grinding disc makes it difficult to control the grinding accuracy, which is an issue that cannot be ignored in the process of grinding RCP.

2.1.1. Research on grinding tool wear processes

The disc grinding process is a highly complex nonlinear process, therefore, the wear forms of the disc during processing are diverse. The grinding disc, sand belt, and grinding wheel all use abrasive particles as cut units, resulting in similar grinding properties. To accurately evaluate the evolution form of the abrasive particle shape within the service life of the disc and establish an accurate model of disc wear, it is necessary to study the wear processes. Research on the wear of grinding tools has reached a consensus to some extent, and the wear stage has been divided into a rapid wear stage and a stable wear stage, e.g., Yan et al. [8] and Pandiyan et al. [9] respectively, who reported that the former stage is related to abrasive fracture and smashing, whereas the latter stage is related to frictional wear of abrasive dullness. Mezghani et al. [10] regarded grinding tools as special multi-blade cutting tools, and their cutting function is mainly completed by abrasive particles adhering to the surface of the substrate. Therefore, at the microscopic level, the wear of grinding tools can be considered the common wear of countless micro-cutting tools. Moreover, considering that grinding discs are rigid grinding tools and that the wear of these rigid grinding tools is somewhat similar to cutter wear from a macro perspective, Nasri et al. [11] and Ulrich et al. [12] provided methods for evaluating the wear of rigid grinding tools. The above research indicates that there is a good

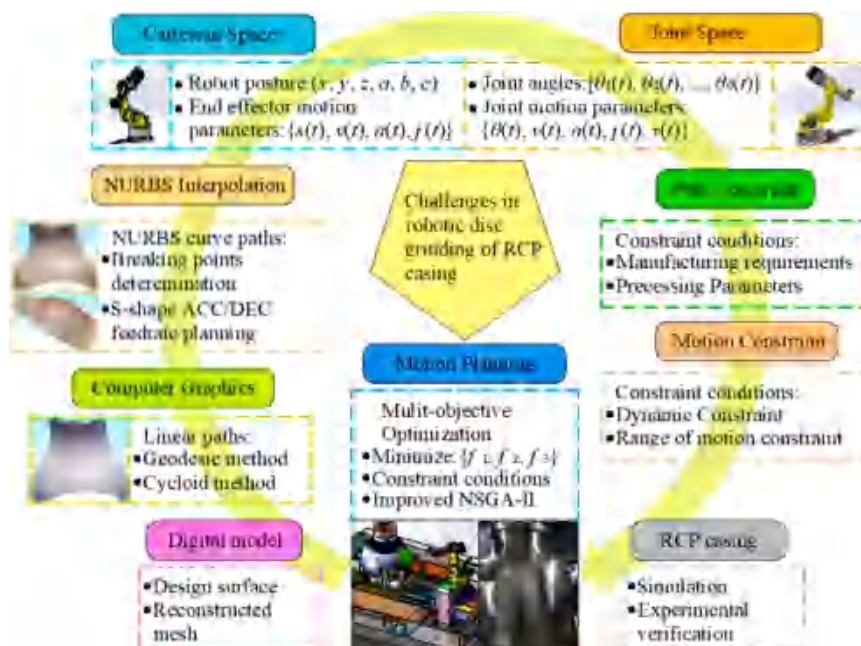


Fig. 1. Schematic diagram of path planning.

correlation between the amount of disc wear and the change in geometric parameters. Disc wear affects the grinding behavior of abrasive particles by changing their geometric parameters, thereby affecting the material removal rate of grinding discs.

2.1.2. Research on the wear prediction model

To accurately control the quality of disc grinding, it is necessary to establish a reliable disc wear model to evaluate the wear status during the grinding process. From a macroscopic perspective, the disc wear capacity represents the wear information, which is generally characterized by the wear quality, height, area, and volume of the disc. At present, scholars have focused on two main directions of research on predictive models for grinding tool wear.

(1) Wear capacity regression model based on machine learning methods.

This type of method establishes regression models by using physical quantities related to grinding tool wear monitored online via modern sensor technology as variables. The grinding tool wear monitoring methods can be classified into two categories: direct and indirect monitoring methods. Online measurement of the former is difficult because of the loss of measuring probes during measurement, whereas the latter often uses visual measurement, sound signal extraction, or thermal energy monitoring devices for data collection and then uses machine learning models to predict the grinding tool wear capacity. Due to the strict requirements of the grinding process on the surrounding environment of the tested object, which may be affected by on-site equipment vibration, dust, and noise, integrating multi-source sensing systems for real-time analysis is often necessary. Therefore, collecting sensitive signals during the grinding process, processing sensor signals, fusing multi-source information, extracting and reducing features, and achieving prediction and recognition on the basis of sensor information are all difficulties in building online monitoring systems. Although many scholars have achieved certain results, their monitoring methods and efficiency still need to be further improved. In particular, the processing of the RCP casing requires the use of a heavy-duty robotic grinding system, which leads to more severe on-site equipment vibration, dust, and noise, all of which increase the difficulty of online monitoring accuracy and efficiency.

(2) Grinding tool wear model based on mathematical analysis.

This type of method is based on traditional mathematical models and further establishes empirical models of grinding tool wear on the basis of experiments. Wang et al. [13] used the finite element method to develop a physical simulator for the abrasive belt grinding process, which uses different contact wheel hardnesses and contact forces to grind titanium alloys. On the basis of finite element analysis, Lu et al. [14] presented a novel dual-axis wheel polishing technique using a semi-rigid polishing wheel, which remodeled the tool influence function and tested the material properties. At present, research has focused mainly on the construction of wear models for flexible or semi-rigid grinding tools, e.g., sand belts tensioned with rubber wheels or resin bonded abrasive particles with aluminum alloy wheels. By establishing a wear process model based on classical theoretical models such as the Archard equation and Hertz elastic contact theory, the relationship between the service life of grinding tools and grinding process parameters can be revealed. The grinding disc mentioned in this paper is classified as a rigid grinding tool because of its ability to ensure a high material removal rate and withstand high grinding pressure during the grinding process. There are relatively few literature reports on the modeling of grinding disc wear models and these rare wear models, to some extent, refer to the wear models of rigid cutting tools.

2.2. Grinding path planning

Path planning methods involve computer graphics, optimization problems, and robotics. From the perspective of computer graphics, the terminology “path planning” refers to the method of planning a series of

specified continuous linear paths [15] or NURBS curve paths [16] along which the robot moves its end effectors (i.e., vision sensor, cutter, and angle grinder) to scan profiles or form the desired surfaces. The continuous linear paths consist of ordered discrete points, while the corresponding NURBS parameter curve paths are obtained through parameterized interpolation. Considering the interference problems of the robot working environment, the limitations of joint motion ranges, and the grinding parameter limitations, research on robotic grinding path planning has focused mainly on common approaches, e.g., the iso-parametric method [17] and the iso-planar method [18]. The former method is based on discretizing surface parameters, whereas the latter method is based on finding the intersections of the cutting planes and the surface. Advanced graphics methods to improve the manufacturing efficiency and quality, e.g., Shahzadeh et al. [19] presented a tolerance constrained G^2 continuous path smoothing and interpolation method for implementing high-speed machining and Hauth et al. [20] used the cycloid curve method to achieve multi-directional paths to eliminate residual scallop heights. The cycloid path is most similar to the circular grinding method used in manual polishing, and it also has the advantages of being smooth and without sharp corners. It can be generated by rolling along a given curve with a circle at a certain point in the plane, and this curve is called the guiding line of the cycloid path [20]. Robotic motion planning (i.e., path planning) methods can generally be divided into Cartesian space path planning [21] and joint space trajectory planning [22]. The Cartesian space path can intuitively and accurately define the position and posture of the robot end effector: first, the intermediate points of the line and arc are obtained by interpolating discrete points, and then the position and posture of the robot end effector are determined via inverse kinematics. There are many calculations in this procedure [23]. Moreover, singular points are inevitable, which makes the joint angle unable to be calculated. In contrast, in joint space, the joint angles are taken as the input values, and the joint curve can be adjusted at any time to avoid the singular value problem [24]. Xu et al. [25] summarized surveys of much more work focused on joint space trajectory planning. Ma et al. [26] noted that joint space trajectory planning needs to consider joint velocity, acceleration, jerk, and other constraints, and it often uses polynomials, S curves, and B-spline curves to construct trajectory curves associated with joint variables.

In the process of practical application, motion planning should not only focus on motion effects and task requirements, but also consider objectives such as efficiency, energy consumption, and impact to find the optimal solution under each working condition [27]. First, processing efficiency is the manufacturer's primary consideration [28]. Early research on robotic path planning carried out trajectory optimization with the goal of shortening the execution time: Dong et al. [29] used quintic non-uniform B-splines to define the joint trajectory and optimized it by implementing particle swarm optimization algorithm. Wang et al. [30] provided a time-optimal piecewise polynomial interpolation trajectory planning algorithm that is based on differential evolution. In addition, for long cycle work, energy consumption has become an important indicator for manufacturers [31]. This is related to robot joint acceleration, which directly affects the smoothness of the trajectory: Zhou et al. [32] proposed a modeling method of energy consumption for industrial robots. The model is a parameterized function constructed by time or joint angle paths and the average acceleration of the end-effector. Moreover, joint impact has become a key indicator for evaluating joint burden and motion stability [33]. Minimizing jerk in joint trajectory planning can effectively reduce joint impact to improve grinding quality. Piazzoli and Visioli [34] used cubic spline curves to perform minimum jerk trajectory planning.

The above-mentioned single type of optimal solution has difficulty meeting the comprehensive requirements of industrial applications. Considering two or more types of optimization methods at the same time is usually a more appropriate trajectory planning scheme for practical applications, i.e., by mixing multiple objectives into one objective for processing [35] or by using multi-objective optimization algorithms

[36]. Weng et al. [37] reported that the multi-objective trajectory planning problem of industrial robots was an NP-hard problem, which was more suitable for using heuristic algorithms. Among many heuristic algorithms, the most commonly used excellent multi-objective meta-heuristics (MOMHs) algorithms are the SPEA2 [37], MOEA/D [38], MOEA/D-DE [39], NSGA-II [40], and MODE algorithms. Bureerat et al. [41] presented self-adaptive multi-objective real-code population-based incremental learning hybridized with differential evolution (MRPBIL-DE) to minimize the travel time and minimize the maximum jerk that occurs during motion. Several MOMHs, along with the proposed algorithm, were used to solve the trajectory optimization problem of robots, and their performances were investigated.

However, to the best of our knowledge, no research has investigated disc wear as an optimization objective. Disc wear will affect the material removal rate, grinding quality, and frequency of grinding disc replacement. With the loss of the grinding disc, the area of the contact disc will gradually increase, thus forming a glaze on the active particles, and the material removal process will stop [12]. Once the grinding disc is replaced, the tool coordinate system needs to be recalibrated, which will affect the grinding time.

This paper describes a robotic disc grinding path planning method based on multi-objective optimization algorithm for RCP casings. In Section 3, a wear model for rigid grinding discs is presented, and its accuracy is evaluated. In Section 4, the conversion process from geodesic offset paths and cycloid paths to NURBS curves is introduced, a time-

jerk-disc wear trajectory optimization model is built, and the optimization results are studied. In Section 5, simulation, verification and analysis are presented. Field implementations of this technology are presented by using a heavy-duty 6-axis articulated KUKA robot—KR 600 R2830. Finally, in Section 6, we present our conclusions and suggest a number of ways in which further research might be pursued.

3. Disc wear model

3.1. Wear model of rigid disc

Considering that the contact area is very small compared with the workpiece, to simplify the problem, it is assumed that the surface curvature over the contact area does not change. As illustrated in Fig. 2, the grinding disk with radius R is tilted by an angle θ , opposite to the feedrate direction, and it contacts the workpiece with tool displacement (represented as L). The contact region, whose shape and size are closely related to L , θ , and surface curvature, is subsequently formed by the arc of the grinding disk boundary \widehat{BDC} and the contact boundary \widehat{BAC} .

Considering that in the actual grinding process, the curvature radius of the contact area is much larger than the radius of the disc and that L is very small (usually not exceeding 3 mm), the influence of the contact model on the contact area can be ignored. In reference [12], the actual contour of the disc during the grinding process was proposed: as the disc wore, the angle of the cutting surface gradually decreased, and the worn

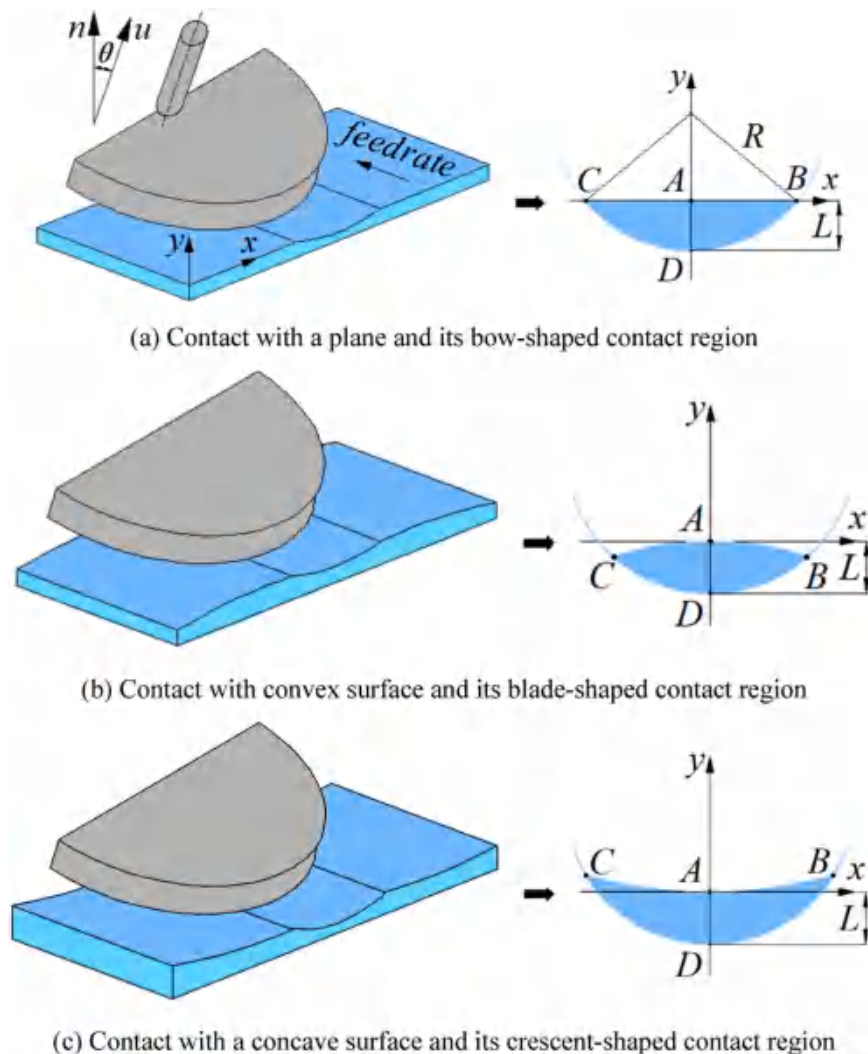


Fig. 2. Contact models of grinding with a tilted rigid disk.

section could be approximated as a triangular cross-section. Therefore, over a short time dt , the triangular area representing the cross-section of the wear volume can be approximated by the sector area in radians:

$$A_w = \frac{L^2 d\theta_i}{2(\sin\theta_i)^2} \quad (1)$$

Considering the different curvatures of the workpiece, the material removal depth L along the grinding path remains unchanged. Therefore, the volumetric wear rate of the disc is obtained by multiplying it by (multiplying by the mean circumference of the disc)

$$Z_s = 2\pi R A_w = \frac{L^2 \dot{\theta}_i (\pi \bullet R)}{(\sin\theta_i)^2} \quad (2)$$

where $\dot{\theta}_i$ is the time derivative of θ_i and θ_i is the disc wear angle.

3.2. FEM simulation

In this work, the static robot stiffnesses are obtained through the experimental method in [42], and the material removal rate (MRR) model for rigid discs is computed via the method in [12]. Moreover, the disc wear model, static robot stiffnesses, and MRR model are combined to construct a grinding force model. During simulation, the horizontal stiffness (z-axis direction) of the grinding system was taken as constant for the entire path, and the vertical stiffness (y-axis direction) was modeled at each point by two linear segments fit through the experimental data. Taking the following experimental parameters, e.g., L is 1.5 mm, the feedrate is 18 mm/s, R is 80 mm, θ is 15° and the disc speed is 8000 rpm, as an example, the simulation results are shown in Fig. 3.

Using the above grinding conditions, the wear model predicted a change of 0.135° in the cutting surface angle during a single grinding

process with a total length of 1.5 m. The actual measured disc wear during this pass was approximately 0.142° . The simulation predicts that the volumetric wear rate of the rigid disc is very close to the experimental values.

Considering that the tracking error was highly reproducible for a given trajectory [43], it was easy to incorporate it into the grinding force simulation by simply adding the data to the reference data. Fig. 4 shows the actual and simulated grinding force patterns for a single grinding pass under incorporated grinding conditions. The simulated predicted grinding forces are very close to the experimental values. Therefore, the wear model of rigid discs can be used for wear prediction.

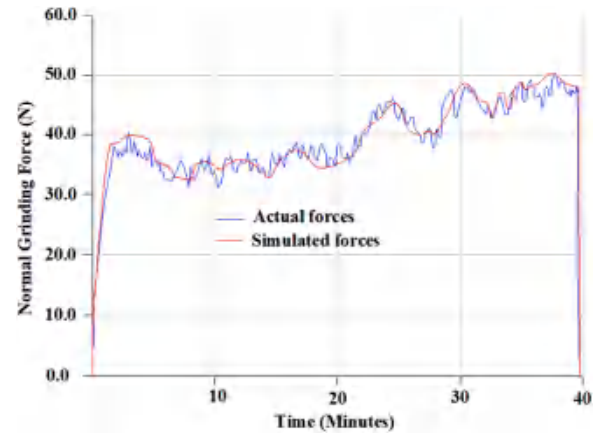


Fig. 4. Actual and simulated normal grinding forces.

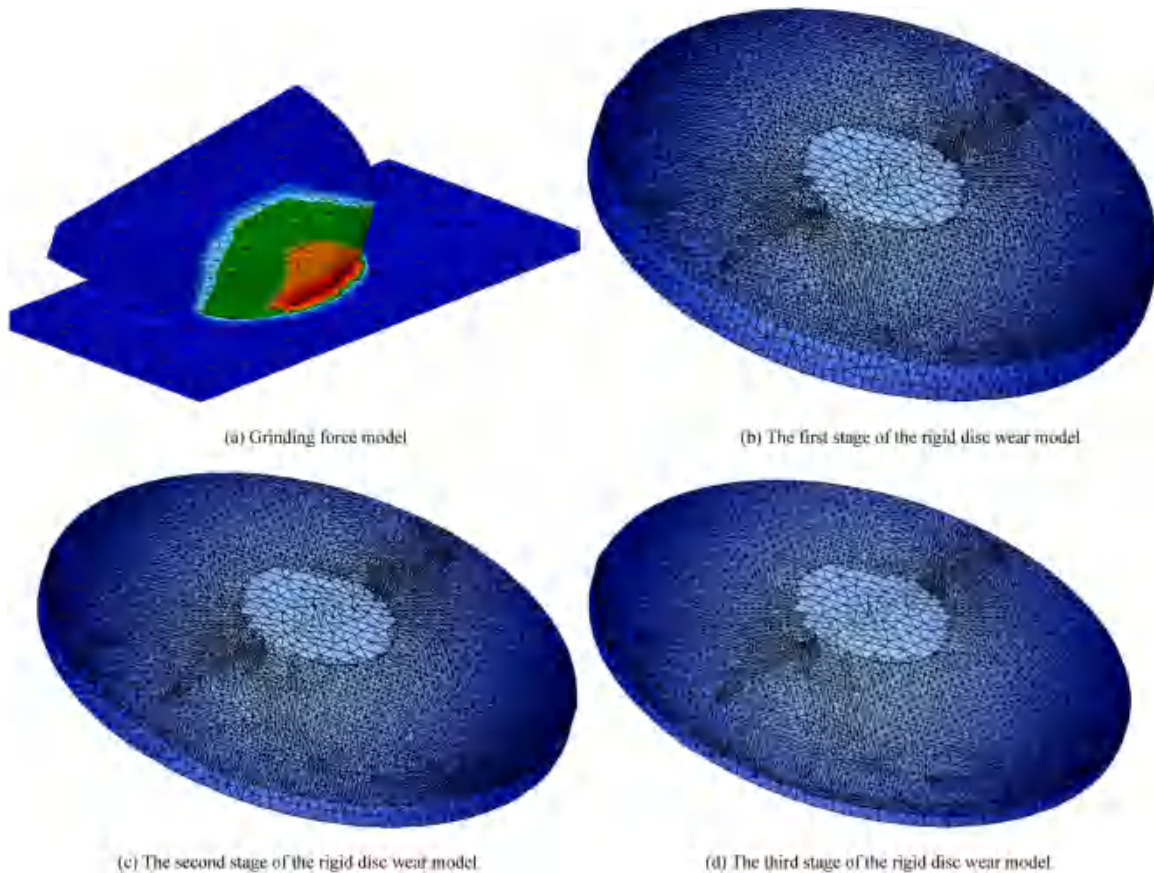


Fig. 3. Simulation results.

4. NURBS curve paths

In many industrial manufacturing fields, a substantial proportion of streamlined shapes are utilized to generate smooth surface profiles. To ensure the accuracy requirements, complex curves with streamlined shapes must be divided into many tiny straight lines or arcs, which not only generate a massive volume of data and reduce the execution efficiency, but also seriously affect the movement speed. Advanced industrial robots, e.g., KUKA and Staubli, provide not only linear motion but also spline motion. In this work, the continuous linear paths that originate from geodesic offset methods are converted to NURBS curve paths.

4.1. Geodesic offset methods

The shortest path between two points on a surface in three-dimensional space is called a geodesic path on the surface and the shortest distance between two points on a surface is called a geodesic distance. Moreover, geodesic offset or parallel paths are a set of points on a surface that maintain a constant geodesic distance from the generator, where the generator is a set of points and polylines restricted on the input triangle mesh [44]. Considering that the geodesic offset path has the characteristic shortest path length, in this paper, the geodesic offset path is taken as the original continuous linear path.

The point cloud of an RCP casing is obtained by a laser scanner and converted into a mesh model via the Poisson reconstruction algorithm proposed by Kazhdan et al. [45]. The calculation of geodesic distances on triangle meshes has many applications, e.g., graph partitioning, parameterization, and tool-path planning [46], yet empirical research is rare if ever cited to support the goal of robot manufacturing work.

In this work, the linear window propagation problem is computed via the method presented in [46]: By setting the intersection results with different values, we can obtain the propagation procedures. As shown in Fig. 5, propagation starts in the central area and spreads to both sides.

Next, we can obtain the whole propagation distance field and connect the points with the same propagation distance value according to the preset specified path interval. To clearly show tool paths, the path interval is set to be much larger than those in real grinding cases. Fig. 6 shows a color map of the propagation distance field and geodesic offset paths of each part of the RCP casing, with an interval of 30 mm.

Moreover, considering the inhibitory effect of multi-directional paths on the grinding texture, we use the cycloid paths proposed by Li et al. [47]. For comparison with the geodesic offset method, cycloid curve paths with an interval of 60 mm are used, i.e., the overlap rate is 50 %. This interval makes the path interval the same as that of the geodesic offset method. Considering that if the mesh model is completely covered by the cycloid curve paths, it will lead to visual confusion, only the paths converted from the source line and its geodesic offset paths on both sides are illustrated in Fig. 7.

As illustrated in Fig. 8a, a method presented by Panozzo et al. [48] is used for determining principal curvatures: it can find a best-fit quadric surface in the neighborhood around each vertex, and analytically calculates the value and direction of the principal curvature on the quadric

surface. By estimating the directions of the maximum and minimum principal curvatures of the patch where the point is located on the continuous linear path, the tangent vector a and corresponding deputy normal vector o of any point can be calculated; the normal vector n is equal to the cross product result of the tangent vector a and deputy normal vector o . These three directions are perpendicular to each other. As illustrated in Fig. 8b and c, to clearly show these three vectors, the step length is set to be much larger than those in real cases.

To describe the position and posture of the robot, the point position p (p_x, p_y, p_z) and tool coordinate system (denoted as T_1) are connected. In contrast to the work piece coordinate system, the translation vector and rotation matrix, which are related to T_1 , can be described by four vectors: let n, o, a (which are used to form a 3×3 rotation matrix) and p' (i.e., a 3×1 translation vector), which restructures a new 4×4 homogeneous transformation matrix M (a 1×4 vector is added as the last row). Moreover, this 3×3 rotation matrix $M_{xyz}(\gamma, \beta, \alpha)$ can be substituted by the RPY (roll, pitch and yaw), which are rotated around mutually perpendicular x, y , and z -axes, respectively, and are denoted as γ, β , and α . The equations of M and $M_{xyz}(\gamma, \beta, \alpha)$ are shown as follows:

$$M = \begin{bmatrix} & p_x \\ M_{xyz}(\gamma, \beta, \alpha) & p_y \\ & p_z \\ 000 & 1 \end{bmatrix} \text{ and } M_{xyz}(\gamma, \beta, \alpha) = \begin{bmatrix} n_{11} & o_{12} & a_{13} \\ n_{21} & o_{22} & a_{23} \\ n_{31} & o_{32} & a_{33} \end{bmatrix} \quad (3)$$

Solving the equivalent rotation angles γ, β , and α around the axes x - y - z from this given rotation matrix $M_{xyz}(\gamma, \beta, \alpha)$ is the inverse solution problem of the RPY angles. Referring to the related content presented by Zhou et al. [15], in the case of $\cos\beta \neq 0$, the arctangent expression of each angle can be written as:

$$\begin{cases} \alpha = \text{atan2}(n_{21}, n_{11}) \\ \beta = \text{atan2}\left(-n_{31}, \sqrt{n_{11}^2 + n_{21}^2}\right) \\ \gamma = \text{atan2}(o_{32}, a_{33}) \end{cases} \quad (4)$$

where atan2 denotes the bivariate arctangent function. In the case of $\beta = \pm 90^\circ$ and $\cos\beta = 0$, the above inverse solution becomes degenerate and the sum value or difference value of α and β can be solved; usually, let α be 0; therefore, the result of the solution is as follows:

$$\begin{cases} \alpha = 0 \\ \beta = \pm \frac{\pi}{2} \\ \gamma = \text{sign}(\beta) \bullet \text{atan2}(o_{12}, o_{22}) \end{cases} \quad (5)$$

where $\text{sign}(\beta)$ sets the sign of γ to be the same as the sign of β .

4.2. NURBS curve interpolation method

The NURBS curve is a general mathematical expression tool. It is a superset of the Bezier curve and B-spline curve and can accurately

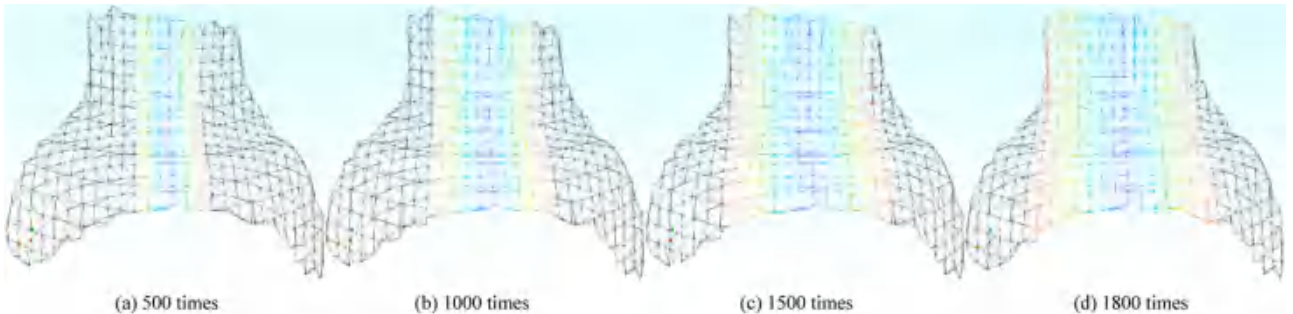
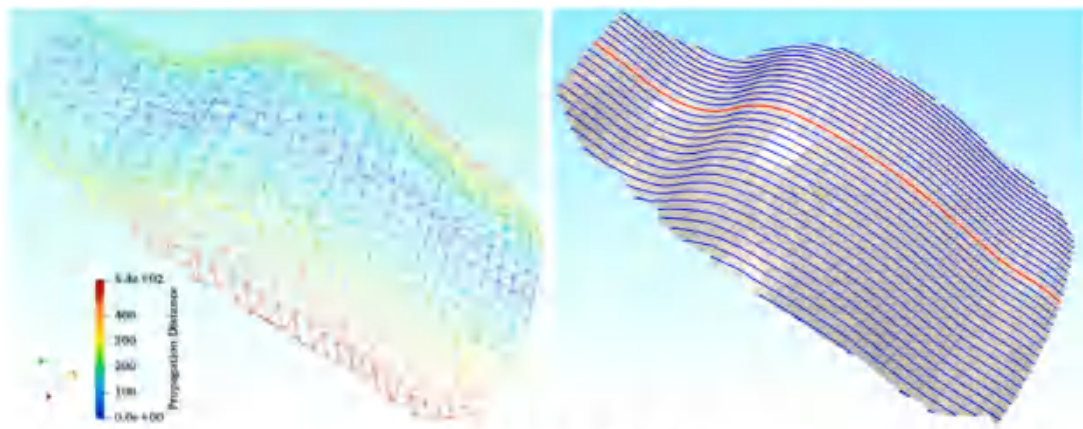
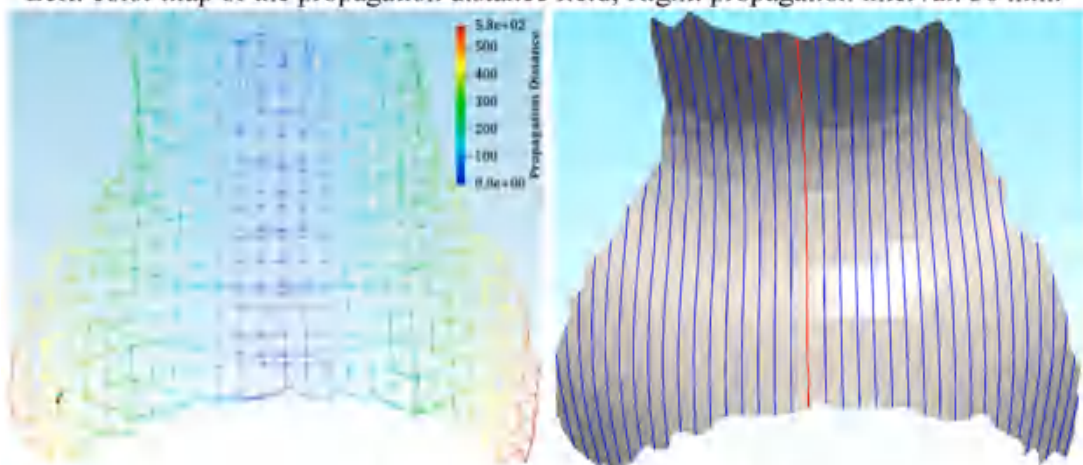


Fig. 5. Propagation procedure with various propagation times.



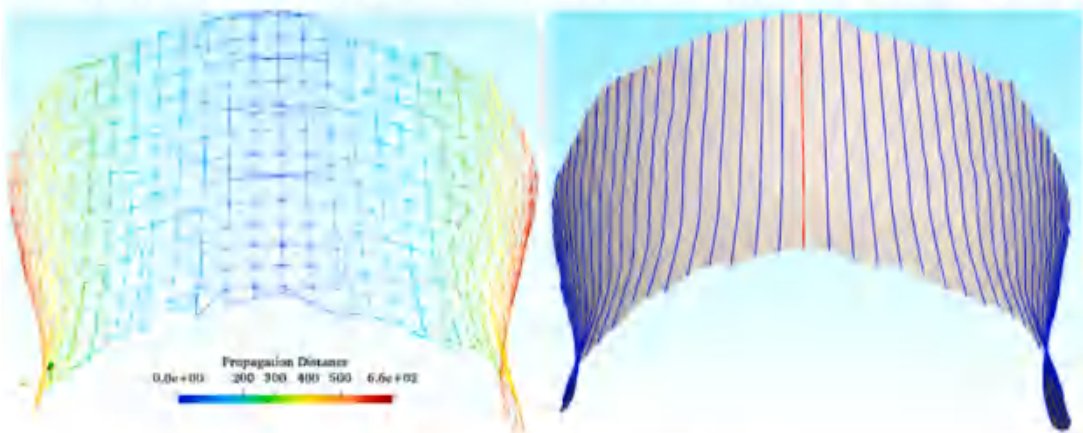
(a) Side face of the RCP casing

Left: color map of the propagation distance field; Right: propagation interval: 30 mm.



(b) Front face of the RCP casing

Left: color map of the propagation distance field; Right: propagation interval: 30 mm.



(c) Output of the RCP casing (upper half)

Left: color map of the propagation distance field; Right: propagation interval: 30 mm.

Fig. 6. Example results demonstrating the suitability of our geodesic offset approach for computing the tool-paths of various parts of the RCP casing, regardless of which surface the region belongs to. (The edge in red denotes the source edge, while the edges in blue denote the tool-paths).

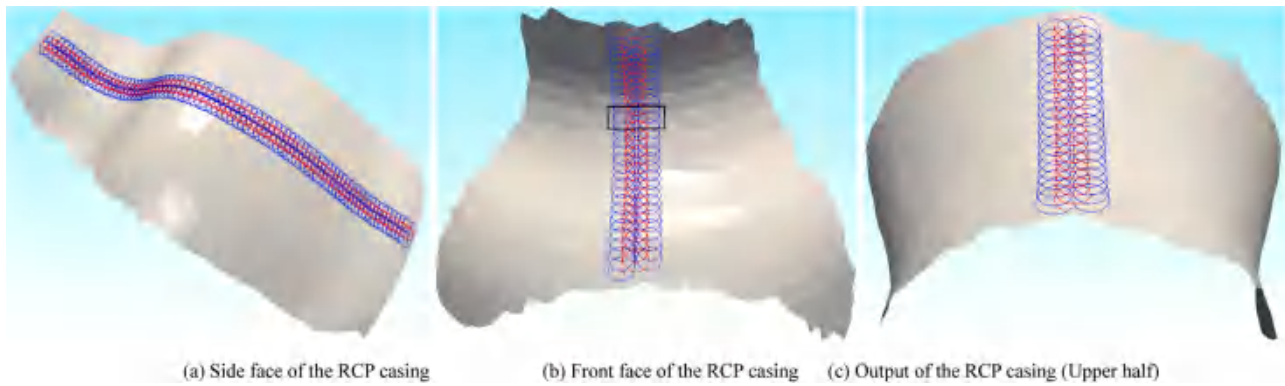


Fig. 7. Example results demonstrating the suitability of our cycloid approach for computing the tool-paths of various parts of the RCP casing, regardless of which surface the region belongs to. (The edges in red denote the cycloid curve paths originating from the source edge, whereas those in blue denote the cycloid curve paths originating from geodesic offset tool-paths).

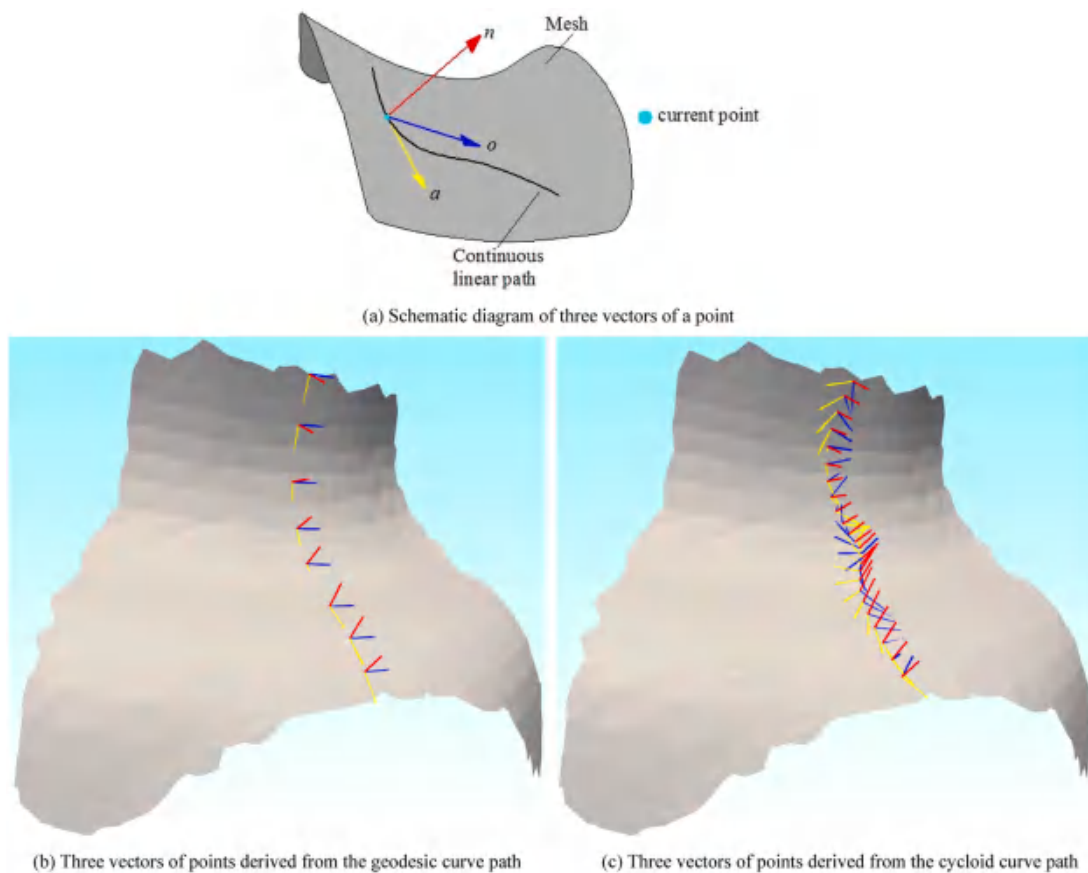


Fig. 8. Path planning and three vectors.

express quadric curves and surfaces. It has been widely used in the field of computer numerical control (CNC) for path planning. In our previous work, Zhou et al. [49] reported that NURBS curve paths not only possess smoothness but also possess the feasibility of replacing many linear paths. Our algorithm can find the breakpoints where the curvature values change abruptly in linear paths and can convert the paths between breakpoints into NURBS curves in real time. Next, for the current NURBS curve, the S-shaped ACC/DEC feed rate planning method is used to make the tool move to the next NURBS curve at the appropriate speed state.

As illustrated in Fig. 9, the geodesic offset paths (as illustrated in Fig. 6) are converted into NURBS paths with colored feed rates according to the S-shaped ACC/DEC feed rate planning method to show

the effectiveness of the algorithm in searching for breakpoints in the paths and the effectiveness of the feed rate planning. Moreover, to clearly show the case of cycloid curve paths, the feed rate planning results in the partial enlargement of Fig. 7b are illustrated in Fig. 10.

5. Multi-objective optimization of robotic disc grinding path planning considering time, jerk, and disc wear

On the basis of previous research on NURBS curve paths, this paper maps the inverse solution of interpolation points in Cartesian space to joint space. The grinding of RCP casings requires not only smooth paths and stable jerk, but also high grinding efficiency and controllable disc wear. The best compromise solution for this problem is the solution to a

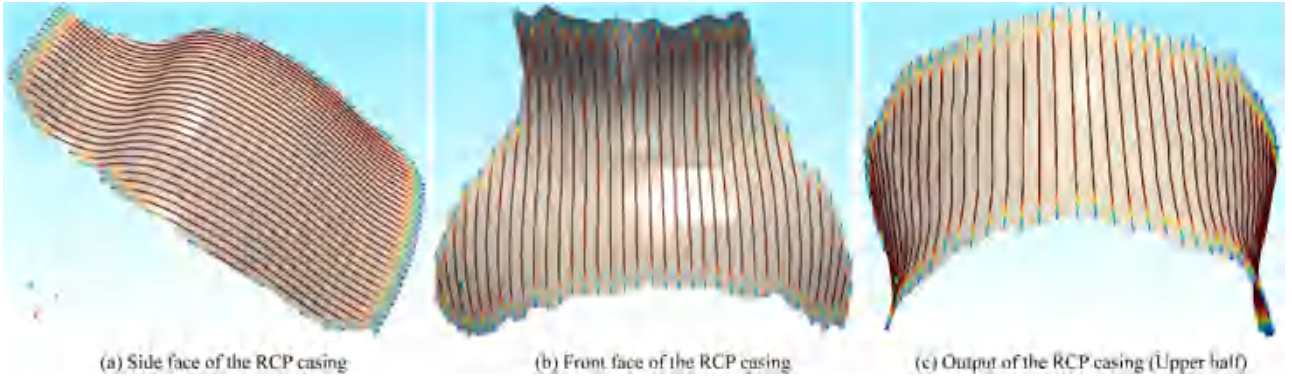


Fig. 9. NURBS trajectories colored according to feedrates.

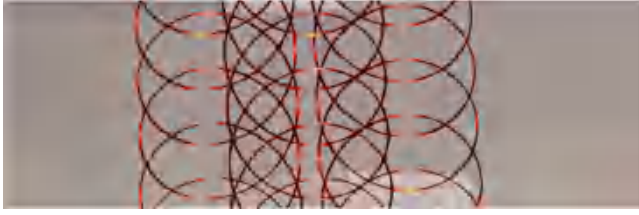


Fig. 10. Partial enlargement of cycloid curve paths.

multi-objective optimization problem. Moreover, considering the complexity of constraints, e.g., accessibility and singularity of position and posture, continuity of angular joint motion, and collision avoidance, the excellent feasible solutions to the proposed problem are randomly distributed in the solution space. In each search process, better solutions may not be found or many unfeasible solutions may be found. The proposed improved NSGA-II algorithm allows the parent population to compete and generate elite strategies for the next generation population, so that the excellent individuals found during the evolution process will not be discarded. It is very suitable for solving the proposed problem and can ensure the reliability of the optimization results.

5.1. Genetic operators in the improved NSGA-II

The implementation of NSGA-II for solving multi-objective optimization problems, it can be divided into three categories [50]: the traditional form without making any changes in the crossover, mutation, and selection operators; the improved NSGA-II, which is based on the selection scheme, crossover and mutation operators, crowding distance operator, constraint handling technique, or other criteria; and the data-driven NSGA-II variant, in which researchers have combined traditional and improved NSGA-II with machine learning techniques. These improvements are often done due to the unsuitability of the traditional NSGA-II for problems in terms of chromosome representation, crossover operator, and mutation operator. The improved and data-driven types aim to improve the efficiency of NSGA-II for a particular problem or a class of problems. Considering that the data-driven type requires extensive experimentation, which increases time and economic costs, this paper adopts an improved NSGA-II method to address the proposed issues.

Crossover, mutation, and selection are the three important operators of genetic algorithms. The traditional NSGA-II uses the simulated binary crossover operator (SBX). However, the global search capability of SBX crossover operator is insufficient, resulting in the inability to ensure population diversity effectively [51]. For two parent individuals $x^{(1,t)}(x_1^{(1,t)}, \dots, x_i^{(1,t)}, \dots, x_n^{(1,t)})$ and $x^{(2,t)}(x_1^{(2,t)}, \dots, x_i^{(2,t)}, \dots, x_n^{(2,t)})$ and

two offspring individuals $x^{(1,t+1)}(x_1^{(1,t+1)}, \dots, x_i^{(1,t+1)}, \dots, x_n^{(1,t+1)})$ and $x^{(2,t+1)}(x_1^{(2,t+1)}, \dots, x_i^{(2,t+1)}, \dots, x_n^{(2,t+1)})$, this paper adopts the normal distribution crossover operator (NDX) with better global search capability [52]:

$$\begin{cases} x_i^{(1,t+1)} = 0.5 \times \left[(1 + 1.481|N(0,1)|)x_i^{(1,t)} \pm (1 - 1.481|N(0,1)|)x_i^{(2,t)} \right] \\ x_i^{(2,t+1)} = 0.5 \times \left[(1 + 1.481|N(0,1)|)x_i^{(1,t)} \mp (1 - 1.481|N(0,1)|)x_i^{(2,t)} \right] \end{cases} \quad (6)$$

where $N(0,1)$ is a normally distributed random variable and is a the uniformly distributed random number in the interval (0, 1).

Moreover, unlike traditional algorithms that use the polynomial mutation operator, this paper adopts Gaussian mutation to improve the efficiency of trajectory planning: most mutation operators are distributed around the original position, which is equivalent to performing neighborhood search within a small range. Moreover, a few operators are far from the current position, enhancing the diversity of the population and facilitating better search of potential areas, thereby improving the search speed and accelerating the convergence trend of the optimization algorithms. The Gaussian probability density formula is as follows [53]:

$$f(x) = \frac{1}{\sqrt{2\pi}\sigma} \exp\left(-\frac{(x-\mu)^2}{2\sigma^2}\right) \quad (7a)$$

where μ represents the average or expected value of the distribution and σ represents the standard deviation. To fully consider the characteristics of the current population, two positions in the population are randomly selected, and the difference between the two is used to interact with the Gaussian distribution operator to form the proposed Gaussian mutation operator. The expression for Gaussian variation is as follows [53]:

$$O = G(\xi) \bullet (X^{\text{rad},1} - X^{\text{rad},2}) \quad (7b)$$

where $G(\xi)$ is a Gaussian distribution formed by the probability density of Eq. (7a), $\xi \in [0,1]$, $X^{\text{rad},1}$ and $X^{\text{rad},2}$ represent the position information of two randomly selected positions in the population, and O represents the Gaussian mutation operator.

Finally, to obtain good distribution in the decision space, the tournament selection operator [50] is adopted to improve the selection operator of NSGA-II.

The parameter values used in the traditional NSGA-II and the improved NSGA-II are shown in Table 1.

5.2. Algorithm validation based on the benchmark test problem suite

The above-mentioned improvements of the NSGA-II need to be

Table 1

Traditional NSGA-II and improved NSGA-II parameters.

Parameters	Values	Description
Population size	100	For three objectives, the number is 300
Crossover probability	0.9	
Selection probability	0.9	
Mutation probability	0.01	
Coefficient of Mutation distribution	20	
Total number of generations	250	
Crossover parameter	10	

validated by comparing it with other advanced algorithms, including the traditional NSGA-II, on the benchmark test problem suite. These algorithms can be divided into two categories on the basis of the evolutionary operator: 1) the proposed improved NSGA-II, traditional NSGA-II, and MOEA/D [38] are based on a genetic algorithm. The first two algorithms are based on the Pareto non-dominated relationship, while the last is based on a decomposition method to decompose a multi-objective optimization problem into a number of scalar optimization problems; 2) OMOPSO and CMPSO are based on the particle swarm optimization (PSO) algorithm [54]. Except for the algorithm proposed in this article, all other algorithms have been proven to be very successful in most multi-objective optimization problems. The main parameter settings of all the compared algorithms are listed in Table 2. The population size and generation number of all five algorithms are set to 300 and 250, respectively.

Three performance indicators, i.e., inverted generational distance (IGD) [55], hypervolume (HV) [56], and the spacing metric (SP) [57], are used to compare the performance of the five algorithms.

The IGD is a comprehensive indicator for measuring the convergence and distribution of the Pareto optimal solution set obtained via an algorithm, as expressed in Eq. (8) [55]:

$$IGD(PF^*, PF) = \frac{\sum_{v \in PF^*} d(v, PF)}{|PF^*|} \quad (8)$$

where PF^* represents the true Pareto optimal frontier, which consists of a series of discrete points evenly distributed on the true frontier; PF represents the Pareto optimal frontier obtained by a certain algorithm; $d(v, PF)$ is the minimum Euclidean distance between v and points in PF , and $|PF^*|$ is the number of members in PF^* . According to Eq. (8), the smaller the IGD value of the Pareto optimal frontier obtained, the closer the solution set is to the true frontier and the more evenly distributed it is.

The HV is used to measure the convergence degree of the Pareto optimal solution set obtained via the multi-objective optimization algorithm, quantifying the difference between the Pareto optimal frontier obtained and the true Pareto optimal frontier, as expressed in Eq. (9) [56]:

$$HV(PF, z^*) = v \left(\bigcup_{u=1}^{|PF|} V(u, z^*) \right) \quad (9)$$

where v represents the Lebesgue measure; $|PF|$ is the number of

members in PF ; u represents an individual in PF , and $V(u, z^*)$ represents the hypervolume between u and the reference point z^* . According to Eq. (9), the smaller the $1/HV$ value of the Pareto optimal frontier obtained, the closer the solution set is to the true frontier and the better the degree of convergence.

The SP is used to evaluate the uniformity of the Pareto optimal solution set distribution obtained via the multi-objective optimization algorithm, as expressed in Eq. (10) [57]:

$$SP(PF) = \sqrt{\frac{1}{|PF| - 1} \sum_{i=1}^{|PF|} (d(u, v) - \bar{d})^2} \quad (10)$$

where $d(u, v) = \min_{v \in PF} \|F(u) - F(v)\|$ represents the Euclidean distance between individual u and its nearest individual v in PF ; $\bar{d} = \frac{1}{|PF|} \sum d(u, v)$ represents the average of these minimum Euclidean distances. According to Eq. (10), the smaller the SP value of the obtained Pareto optimal solution set is, the more uniform the distribution of the solution set.

Table 2 lists the values of the performance metrics (for 30 independent runs) of the utilized multi-objective algorithms in the optimization of DTLZ tri-objective benchmark functions.

These five algorithms are tested on standard tri-objective benchmark test functions [58], e.g., DTLZ1, DTLZ2, and DTLZ7, as listed in Table 3. The bold values in the table represent the best values obtained by the utilized algorithms for each benchmark function.

The first line of each benchmark is the average value of the IGD, $1/HV$, and SP indicators, and the second line is the standard deviation. The proposed algorithm achieves over half of the optimal values, while also achieving a certain proportion of suboptimal values.

In terms of the IGD indicator, the improved NSGA-II performs well in all three objective benchmark functions: among them, the results achieved in DTLZ1 and DTLZ2 are the best, whereas the results achieved in DTLZ7 are second only to those of the OMOPSO algorithm. Therefore, by adopting more suitable crossover, mutation, and selection operators, the improved NSGA-II can find the non-dominant solution with the minimum distance from the Pareto optimal solution and has a better distribution than the other four algorithms do. The proposed algorithm has improved the optimization performance of the traditional NSGA-II algorithm to a certain extent.

Similarly, for both the $1/HV$ and the SP indicators, the improved NSGA-II demonstrates its superiority in almost all aspects. This indicates that the solution set has good distribution uniformity, is closer to the true boundary, and has good convergence.

To further compare these algorithms, the Pareto fronts of the DTLZ test suite obtained by these algorithms are shown in Fig. 11. For the benchmark functions DTLZ1 and DTLZ2, the proposed improved NSGA-II algorithm and MOEA/D algorithm obtained more accurate results, both of which were very close to the optimal Pareto front. However, the improved NSGA-II algorithm achieves a better distribution in DTLZ2: compared with MOEA/D, the improved NSGA-II algorithm can generate better distribution and propagation results for non-dominant solutions. Among these algorithms, the performance demonstrated by OMOPSO and SMPSO is not ideal in most aspects. However, for the DTLZ7 benchmark function, compared with the improved NSGA-II algorithm, the solution obtained by the OMOPSO algorithm is closer to the optimal Pareto front. Nevertheless, the improved NSGA-II algorithm has also achieved suboptimal results. In addition, for this benchmark function, the traditional NSGA-II algorithm obtained better solutions than did the MOEA/D and SMPSO algorithms.

5.3. Problem statement on optimization objectives and constraints

The traveling time (f_1), the jerk of the actuators (f_2), and the disc wear (f_3) are regarded as objectives. The optimization model is formulated as follows:

Minimize:

Table 2

Main parameter settings of all compared algorithms.

Algorithms	Parameter settings
MOED/D	Differential scaling factor $F=0.5$; Crossover probability $CR=0.5$; Mutation probability $p_m=0.01$; Neighbor size $T=20$; Variation distribution coefficient $\eta_m=20$
OMOPSO	Inertial weight coefficient $w \in [0.1, 0.5]$; Acceleration constant $c_1, c_2 \in [1.5, 2.5]$
CMPSO	Inertial weight coefficient $w \in [0.1, 0.5]$; Acceleration constant $c_1, c_2 \in [1.5, 2.5]$

Table 3

Comparison of the 5 algorithms on three performance indicators with average and standard deviations.

Function	Indicator		Improved NSGA-II	Traditional NSGA-II	MOEA/D	OMOPSO	CMPSO
DTLZ1	IGD	Average	4.372E-02	7.032E-02	5.733E-02	3.703E+01	8.007E-02
		Std.	7.817E-04	8.052E-03	1.743E-03	8.98E+00	2.988E-03
	1/HV	Average	5.449E-01	5.437E-01	6.943E-02	8.174E-02	8.30E-02
		Std.	2.281E-04	2.966E-05	1.879E-04	4.145E-05	3.530E-03
	SP	Average	1.67E-02	8.475E-01	1.276E-01	3.691E-02	9.540E-01
		Std.	4.10E-04	5.016E-01	1.940E-01	1.862E-02	4.157E-01
DTLZ2	IGD	Average	4.176E-02	6.955E-02	6.937E-02	4.30E-02	7.077E-02
		Std.	9.571E-04	4.219E-03	1.931E-03	1.337E-03	1.092E-03
	1/HV	Average	3.314E-01	3.743E-01	3.723E-01	3.203E-01	5.152E-02
		Std.	2.64E-02	5.606E-02	7.050E-02	7.837E-03	2.810E-02
	SP	Average	5.99E-03	3.202E-01	2.033E-01	1.175E-02	6.231E-02
		Std.	1.80E-03	1.407E-02	1.220E-02	4.805E-03	3.473E-02
DTLZ7	IGD	Average	3.622E-02	4.621E-01	1.690E-01	2.598E-02	5.269E-01
		Std.	2.867E-02	2.174E-01	1.529E-01	1.681E-03	7.835E-02
	1/HV	Average	3.376E-01	2.321E-01	7.123E-01	4.872E-01	3.181E-01
		Std.	1.138E-02	8.434E-03	3.718E-02	1.327E-02	5.445E-03
	SP	Average	2.843E-01	2.696E-01	2.138E-01	2.673E-01	2.701E-01
		Std.	1.059E-02	3.126E-01	3.672E-02	3.743E-02	3.366E-01

$$f_1 = \sum_{i=0}^{n-1} \Delta t_i = \sum_{i=0}^{n-1} (t_{i+1} - t_i) = T \quad (11a)$$

$$f_2 = \sum_{m=1}^6 \sqrt{\frac{1}{T} \int_0^T (j_m)^2 dt} \quad (11b)$$

$$f_3 = \int_0^T \int_{\theta_0}^{\theta_t} Z_s d\theta_t dt = \int_0^T \int_{\theta_0}^{\theta_t} \frac{L^2(\pi \bullet R)}{(\sin \theta_t)^2} d\theta_t dt$$

$$= L^2(\pi \bullet R) \int_0^T (\cot \theta_0 - \cot \theta_t) dt \quad (11c)$$

where f_1 is the function of consumed time to estimate the working efficiency of the grinding robot; $t_{i+1} - t_i$ represents the time consumed from the i -th parameter point of the NURBS path to the $(i+1)$ -th parameter point; f_2 is the average pulse function of all joints, which is used to estimate the running stability of the grinding robot; j_m represents the joint jerk of the m -th joint; f_3 is the disc wear function used to estimate the volumetric wear of the grinding disc; and $(\cot \theta_0 - \cot \theta_t)$ represents the difference between the angle cosine values before and after grinding disc wear. Considering that when the instantaneous angle of the cutting surface θ_t is close to approximately 2° to 3° [12] (the grinding plate is worn to the glazed appearance), the material removal depth decreases rapidly, and the inclination angle θ_0 of the grinding disc is usually set from 5° to 25° , the cosine difference here can be obtained from the prediction of the wear model to estimate the effective material removal stage of the grinding disc. More accurate values of θ_0 and θ_t can be obtained through experiments. Due to the performance parameters and production cycle limitations of robots, these constraints must be considered when seeking optimization solutions:

Subject to (continued):

$$\theta_m(t) \in \Omega_m \text{ for } m = 1, 2, \dots, 6 \quad (12)$$

$$|v_m(t)| \leq v_{m,\max} \text{ for } m = 1, 2, \dots, 6 \quad (13)$$

$$|a_m(t)| \leq a_{m,\max} \text{ for } m = 1, 2, \dots, 6 \quad (14)$$

$$|j_m(t)| \leq j_{m,\max} \text{ for } m = 1, 2, \dots, 6 \quad (15)$$

$$|\tau_m(t)| \leq \tau_{m,\max} \text{ for } m = 1, 2, \dots, 6 \quad (16)$$

$$T \leq T_{\max} \quad (17)$$

where, m represents the joint number; Ω_m denotes the joint range of joint m ; $v_{m,\max}$, $a_{m,\max}$, $j_{m,\max}$, and $\tau_{m,\max}$ represent the maximum speed, maximum acceleration, maximum jerk, and maximum torque of joint m ,

respectively; T denotes the traveling time of the robot end effector from the initial configuration to the final robot configuration; and T_{\max} denotes the maximum processing time.

Moreover, according to the inverse kinematics solution, the S -shaped ACC/DEC feedrate planning results [49] can be converted to the corresponding speed, acceleration, and jerk of each joint in the joint space:

$$\Delta \theta_i^{(m)} = P^{(m)}(u_i) - P^{(m)}(u_{i-1}) \text{ for } m = 1, 2, \dots, 6 \text{ and for } i = 1, 2, \dots, n \quad (18a)$$

$$t_{i,\min}^{(\omega)} = \max \left\{ \Delta \theta_i^{(m)} / \omega_{\max}^{(m)} \right\} \quad (18b)$$

$$t_{i,\min}^{(a)} = \max \left\{ \sqrt{2 \Delta \theta_i^{(m)} / a_{\max}^{(m)}} \right\} \quad (18c)$$

$$t_{i,\min}^{(j)} = \max \left\{ \sqrt[3]{6 \Delta \theta_i^{(m)} / j_{\max}^{(m)}} \right\} \quad (18d)$$

$$t_{i,\min}^{(a\omega,\omega)} = \max \left\{ \omega_{\max}^{(m)} / a_{\max}^{(m)} + \left(\Delta \theta_i^{(m)} - \omega_{\max}^{(m)2} / (2a_{\max}^{(m)}) \right) / \omega_{\max}^{(m)} \right\} \quad (18e)$$

$$t_{i,\min}^{(ja\omega,\omega)} = \max \left\{ \sqrt{\omega_{\max}^{(m)} / j_{\max}^{(m)}} + \left(\Delta \theta_i^{(m)} - \omega_{\max}^{(m)2/3} / (6j_{\max}^{(m)5/3}) \right) / \omega_{\max}^{(m)} \right\} \quad (18f)$$

$$t_{i,\min}^{(ja\omega,a)} = \max \left\{ a_{\max}^{(m)} / j_{\max}^{(m)} + \sqrt{2 \left(\Delta \theta_i^{(m)} - a_{\max}^{(m)3} / (6j_{\max}^{(m)2}) \right) / a_{\max}^{(m)}} \right\} \quad (18g)$$

$$t_{i,\min}^{(ja\omega,a\omega)} = \max \left\{ a_{\max}^{(m)} / j_{\max}^{(m)} + \omega_{\max}^{(m)} / a_{\max}^{(m)} + \left(\Delta \theta_i^{(m)} - a_{\max}^{(m)3} / (6j_{\max}^{(m)2}) - \omega_{\max}^{(m)2} / (2a_{\max}^{(m)}) \right) / \omega_{\max}^{(m)} \right\} \quad (18h)$$

$$t_{i,\min}^{(m)} = \max \left\{ t_{i,\min}^{(\omega)}, t_{i,\min}^{(a)}, t_{i,\min}^{(j)}, t_{i,\min}^{(a\omega,\omega)}, t_{i,\min}^{(ja\omega,\omega)}, t_{i,\min}^{(ja\omega,a)}, t_{i,\min}^{(ja\omega,a\omega)} \right\} \quad (19)$$

$$t_{i,\max}^{(m)} = kt_{i,\min}^{(m)} \quad (20)$$

For a given NURBS path curve $P(u)$, where u is the interpolation parameter and $n+1$ is the number of control points; $\Delta \theta_i^{(m)}$ denotes the distance of the i -th NURBS path of the m -th joint; Eqs. (18a)–(18h) denote the shortest time required for the i -th NURBS path when performing 1) uniform linear motion; 2) uniform acceleration motion; 3) plus-acceleration motion; 4) uniform acceleration until the angular velocity reaches the maximum value and then executes uniform linear

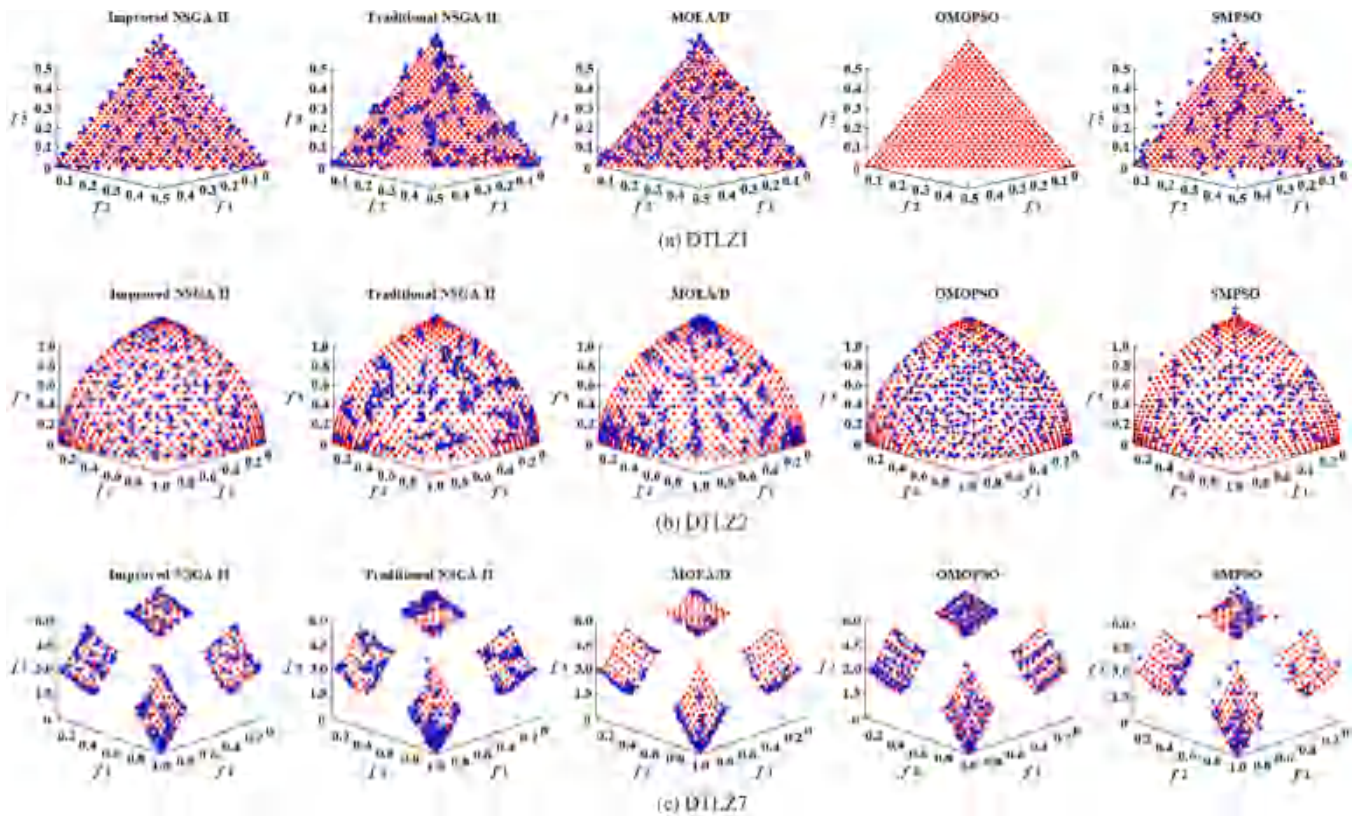


Fig. 11. Pareto front of the DTLZ test suite.

motion; 5) plus-acceleration until the angular velocity reaches the maximum value and then executes uniform linear motion; 6) plus-acceleration until the angular velocity reaches the maximum value, and then executes uniform acceleration motion; and 7) plus-acceleration-uniformly acceleration-uniformly linear motion; $t_{i,\min}^{(m)}$ represents the lower limit of the running time of the i -th NURBS path, which is obtained from the minimum running time of these seven motions; and $t_{i,\max}^{(m)}$ represents the upper limit value, which is k times that of $t_{i,\min}^{(m)}$. If the value is set too small, the optimization results cannot be solved; if the value is set too large, it will lead to lower computational efficiency. Under the feedrate conditions mentioned in this work, by performing simulation calculations, an appropriate empirical value is obtained such that k is equal to 5.

By substituting the above optimization objectives, constraints, and genetic operation into the improved NSGA-II algorithm, the robot trajectory optimization task can be started.

5.4. Optimization results analysis

The kinematic constraints of the KUKA robot (Type: KR 600 R2830) are shown in Table 4. According to the joint angles and kinematics constraints in Table 4, the lower and upper limit values of the design variables can be calculated according to Eq. (20).

We selected partial NURBS curve paths originating from the geodesic offset and cycloid paths, as shown in Fig. 12. Their lengths are 100.32 mm and 100.29 mm, respectively. The path planning effects corresponding to the median solutions are shown in Fig. 13 and Fig. 14.

The optimized paths can not only meet the kinematic constraints of the robot, but also have smooth and continuous joint velocities, continuous joint accelerations and small joint jerks. These excellent characteristics can ensure path stability, have little impact on the joint, and prolong the service life of the disc. However, even if the path length is close to the same, compared with the one-directional paths, the multi-

directional paths, e.g., optimized cycloid paths, will produce varying grinding contact forces and varying disc sliding velocities, which will lead to more complex material removal situations. The establishment condition of Z_s cannot be guaranteed; therefore, this leads to large calculation errors, thus significantly extending the grinding time.

The path planning effects corresponding to the optimal solutions are shown in Fig. 15 and Fig. 16. The contours of the joint angle curves are essentially the same, but the time-consumption is different.

Compared with the one-directional paths, the grinding time of each optimal solution of the multi-direction paths is also significantly prolonged. This finding also verifies our conjecture that the multi-directional paths will destroy the establishment condition of Z_s and that large calculation errors affect the accuracy of the optimization solution.

Therefore, we analyze only the optimization results of the geodesic offset paths. Compared with those of the time-optimal paths, the velocity, acceleration and jerk of the impact-optimal paths are reduced by 50 %, 90 % and 95 %, respectively, whereas compared with those of the disc wear-optimal paths, the corresponding values are reduced by 60 %, 92.5 % and 96 %, respectively. Table 5 shows that the eclectic solution is longer than the time-optimal solution by more than 20 %, but the jerk is reduced by more than 60 %. Compared with the disc wear-optimal

Table 4
Kinematic constraints of KUKA robot—KR 600 R2830.

Serial number	Joint constraints					
	Joint 1	Joint 2	Joint 3	Joint 4	Joint 5	Joint 6
$\theta_{\max}(\text{rad})$	3.227	0.349	2.512	6.106	2.093	6.106
$\theta_{\min}(\text{rad})$	−3.227	−2.268	−1.744	−6.106	−2.093	−6.106
$\omega(\text{rad/s})$	1.396	1.308	1.221	1.221	1.221	1.919
$\alpha(\text{rad/s}^2)$	4.74	4.74	6.85	6.85	6.85	6.85
$j(\text{rad/s}^3)$	33.57	33.57	52.36	52.36	52.36	52.36
$\tau(\text{Nm})$	1000	1000	1000	1700	1700	1000

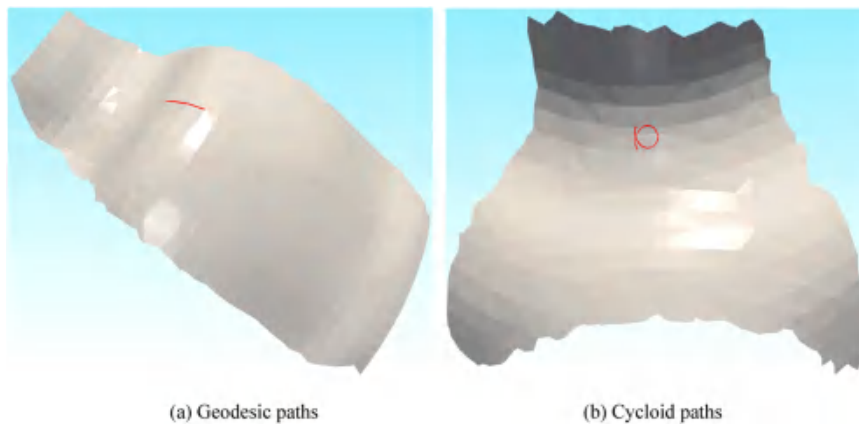


Fig. 12. Parts of the NURBS curve paths.

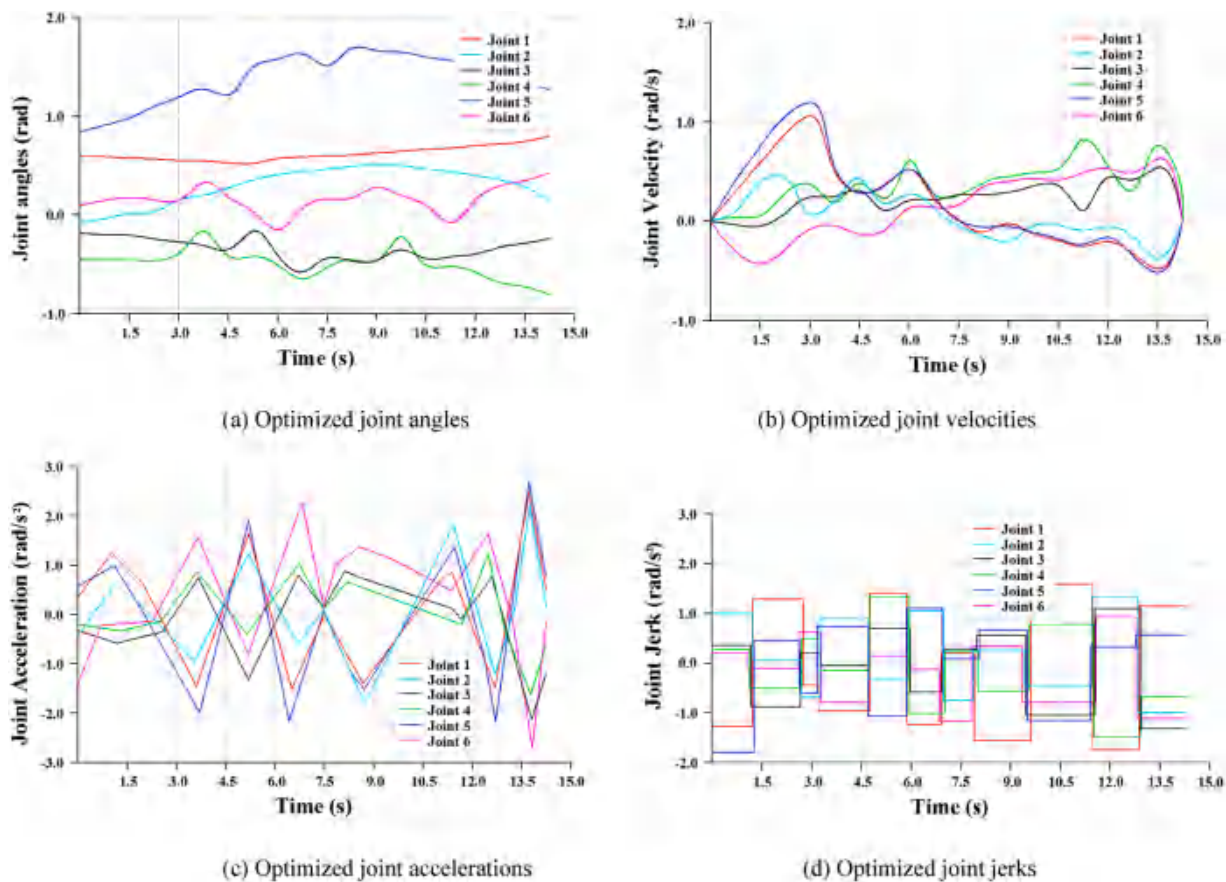


Fig. 13. Optimized results of the geodesic paths.

paths, the disc wear target of the eclectic paths is only increased by less than 5 %, but the running time is reduced by 70 %.

6. Simulation, verification and analysis

According to the manufacturing requirements and the dimensions of the RCP casing, to evaluate the proposed algorithm, the whole work piece must be divided into upper and lower halves to perform grinding work. Considering the rotary structure of the pump body and the reachable range of the robot, the tasks of grinding and detection analysis should be carried out at 30° intervals. The grinding and evaluation stages involved in this new technology are illustrated in Fig. 17. The scanning process uses geodesic offset paths, whereas the grinding

process uses not only geodesic offset paths but also cycloid paths. After grinding the current region, it is necessary to scan the grinding region, convert the scanning data to the model coordinate system, and analyze the grinding errors. The local grinding areas that exceed the grinding errors need to implement grinding until the grinding errors of the current region meet the manufacturing requirements. The scanning data were subsequently collected and merged for overall analysis. After completing the whole grinding task, we performed precision, accuracy, and stability analyses and further optimized the grinding parameters. The robot relies on a hybrid force/position controller to ensure the contact condition of Z_s during the grinding process between the grinding disc and the workpiece. The Tool-Changer system can provide a flexible automation process for replacing line-structure light sensors and angle

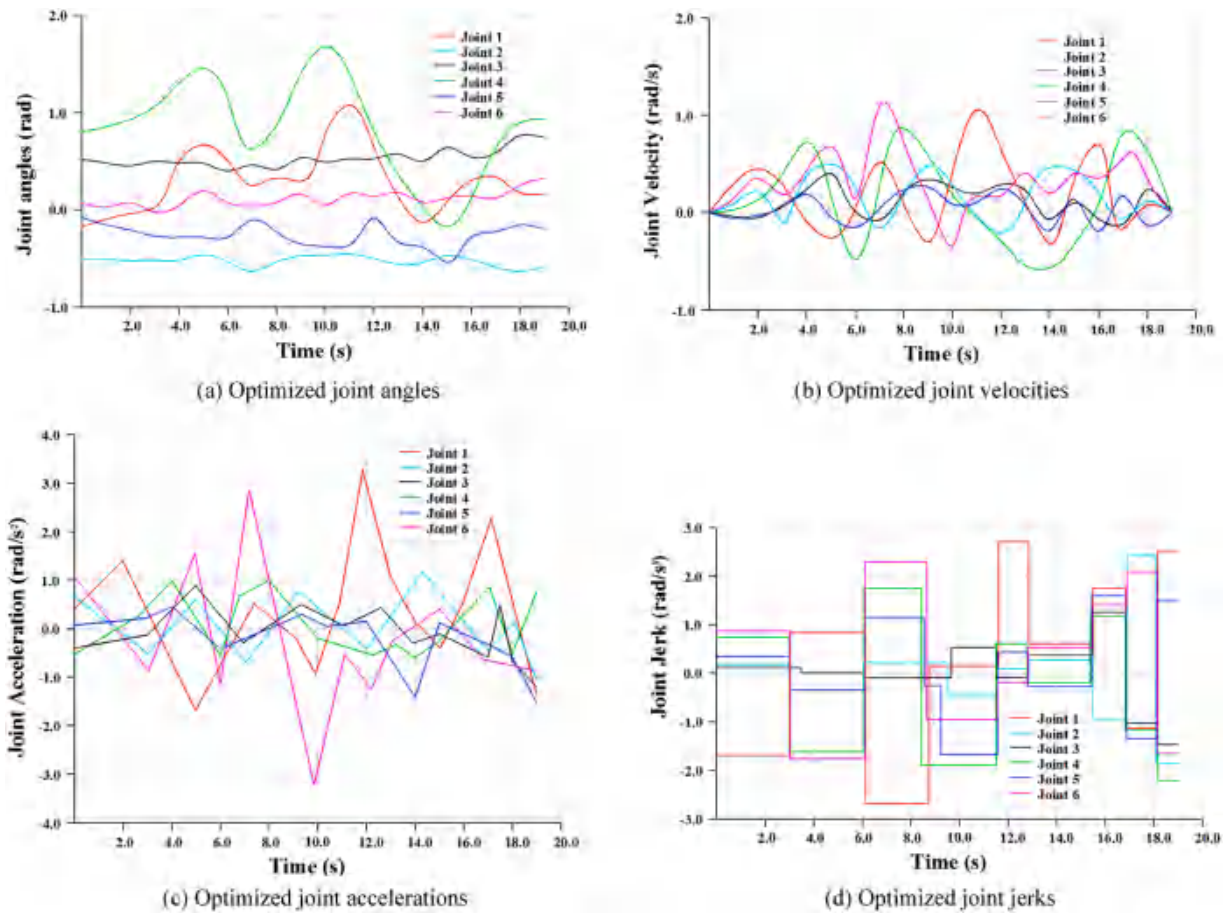


Fig. 14. Optimized results of the cycloid paths.

grinders. In this work, the removal depth was set to 0.6 mm, which was based on the empirical value summarized from manual grinding tasks.

6.1. Simulation

Simulation is the preliminary operation for manufacturing parameter testing and adjustment and can provide an intuitive testing environment for the motion planning of real robots. In the simulation process, a series of steps similar to those of actual manufacturing work need to be performed. After loading the robot and its environment, three key issues need to be considered:

- 1) Collision inspection, including: not only collision detection between tools and work pieces, but also collision detection between robots and work pieces; 2) processing parameter selection, including: normal direction, path interval, and step length; and 3) accessibility inspection, including reachability judgment of the robot, paths corresponding to the coverage of the region to be ground, and wrist singularity.

To provide a clearer explanation, we number the region following the processing sequences from top to bottom, as illustrated in Fig. 18.

After the simulation functions for collision inspection and accessibility inspection are implemented, the grinding parameters are formulated as shown in Table 6. Notably, for different regions to be ground, a wider grinding range can be polished by properly associating the coordinate system of the angle grinder, such as the bottleneck area near the lifting lug: without changing any grinding parameters, the grinding task of this region can be realized only by switching the coordinate systems of the angle grinder. Table 5 contains these tool coordinates (i.e. T1, T0 and T2), and there is a 90° equiangular spacing relationship between them.

In Table 6, T1/ T2 denotes that the corresponding regions can be

ground by using the T1 or T2 tool coordinate system; T0 & T1 (or T0 & T2) indicate that the corresponding regions can be ground by switching the T0 and T1 tool coordinate systems. For example, the inlet region (upper half) can be ground in the T1/T2 tool coordinate system, and the outlet domain (lower half) can be ground in the T0 tool coordinate system. The grinding work simulation is illustrated in Fig. 19. To clearly show the grinding paths, the error criterion (i.e., path interval) is set to be much greater than those in real cases.

- ① Tool-path editor functions, including load, play, save and modify, etc. ② Collision inspection with additional functions, including: highlighting and removing collision positions, etc. ③ Grinding simulation and rendering ④ Position and posture in Cartesian space ⑤ Joint angles in joint space ⑥ External axes input.

Moreover, taking the three source edges in Fig. 6 as paths to be evaluated, the optimization parameters are set according to Table 1 and Table 2. The kinematic constraint transformation method proposed in Chapter 4 (Eqs.(18)-(20)) is adopted for constraint processing, which transforms the robot kinematic constraints into the upper and lower limits of the design variables for the time-jerk-disc wear optimization problem. Fig. 20 shows the boxplots of the *IGD*, *1/HV*, and *SP* indicators derived from 30 independent runs of the proposed improved NSGA-II, traditional NSGA-II, MOEA/D, OMOPSO and CMPSO algorithms in solving the proposed multi-objective problem.

The boxplot of the improved NSGA-II algorithm is very narrow and is located below the minimum values of other algorithms. The MOEA/D showed the second best result, followed by the traditional NSGA-II, and their performances were similar to each other. It can be concluded that the proposed improved NSGA-II algorithm performs the best on all the three test paths according to the *IGD*, *1/HV*, and *SP* values and is significantly difference from the other algorithms. Moreover, the *SP*

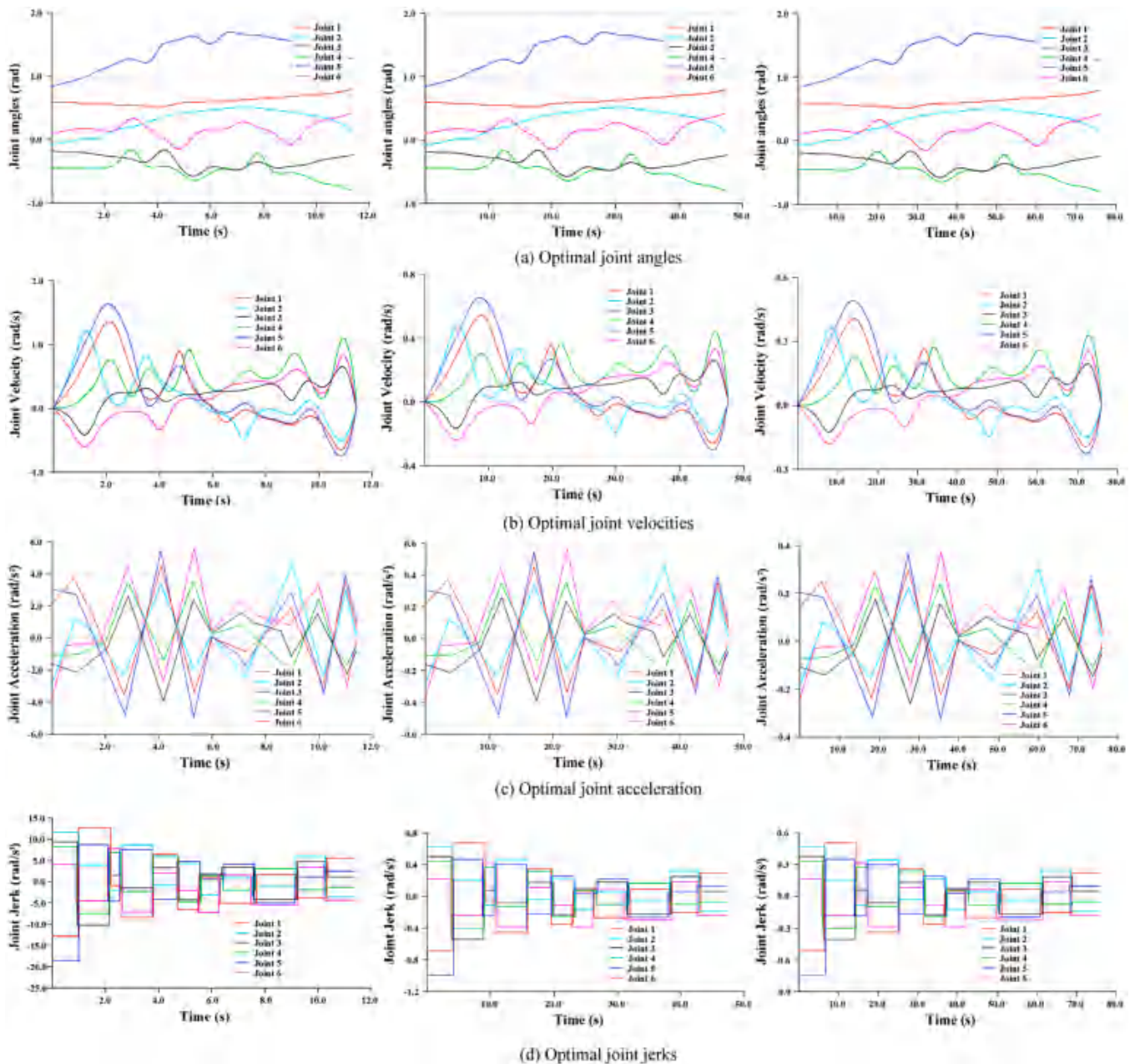


Fig. 15. Optimal results of the geodesic paths (from left to right represent time, impact, and disc wear aspects).

boxplot has the lowest and narrowest appearance, indicating that the proposed algorithm has the highest efficiency in solving the multi-objective optimization problem. Due to the use of the same constraints, multi-objective functions, and parameter setting, the boxplots corresponding to the three paths have a certain degree of similarity, and the number of points sampled on each path determines the values.

To further analyze the convergence behavior of all these algorithms, taking the first path as an example, Fig. 21 shows the relationship between the average *IGD* results obtained by all these algorithms and the iteration times for each optimization problem. The convergence curve indicates that the proposed algorithm can effectively avoid premature convergence and evolutionary stagnation. On the basis of the comprehensive analysis of Figs. 20 and 21, the proposed algorithm performs the best in the proposed multi-objective optimization problem.

6.2. Experimental verification

First, we follow the grinding sequences and grinding parameters referred to in the simulation experiments. Then, we generate grinding paths from the simulation module and insert corresponding codes in the robot executable file. By using a noncontact measuring system (line-structure light equipment, type: Micro-Epsilon LLT 2600–100), we can obtain scanning data with a measurement accuracy of 10–100 μm . The stainless steel type of the RCP casing is CF8M, and the Brinell hardness is nearly 183 HBW.

The simulation process can increase our understanding of scanning and grinding processes and promote the development of our optimization algorithms. To realize the practicality of this technology, it is necessary to perform actual grinding. First, we use the simulation grinding parameters shown in Table 6 to perform the corresponding commissioning work. This commissioning work can determine whether the scanning or grinding paths can cover the desired regions, and avoid

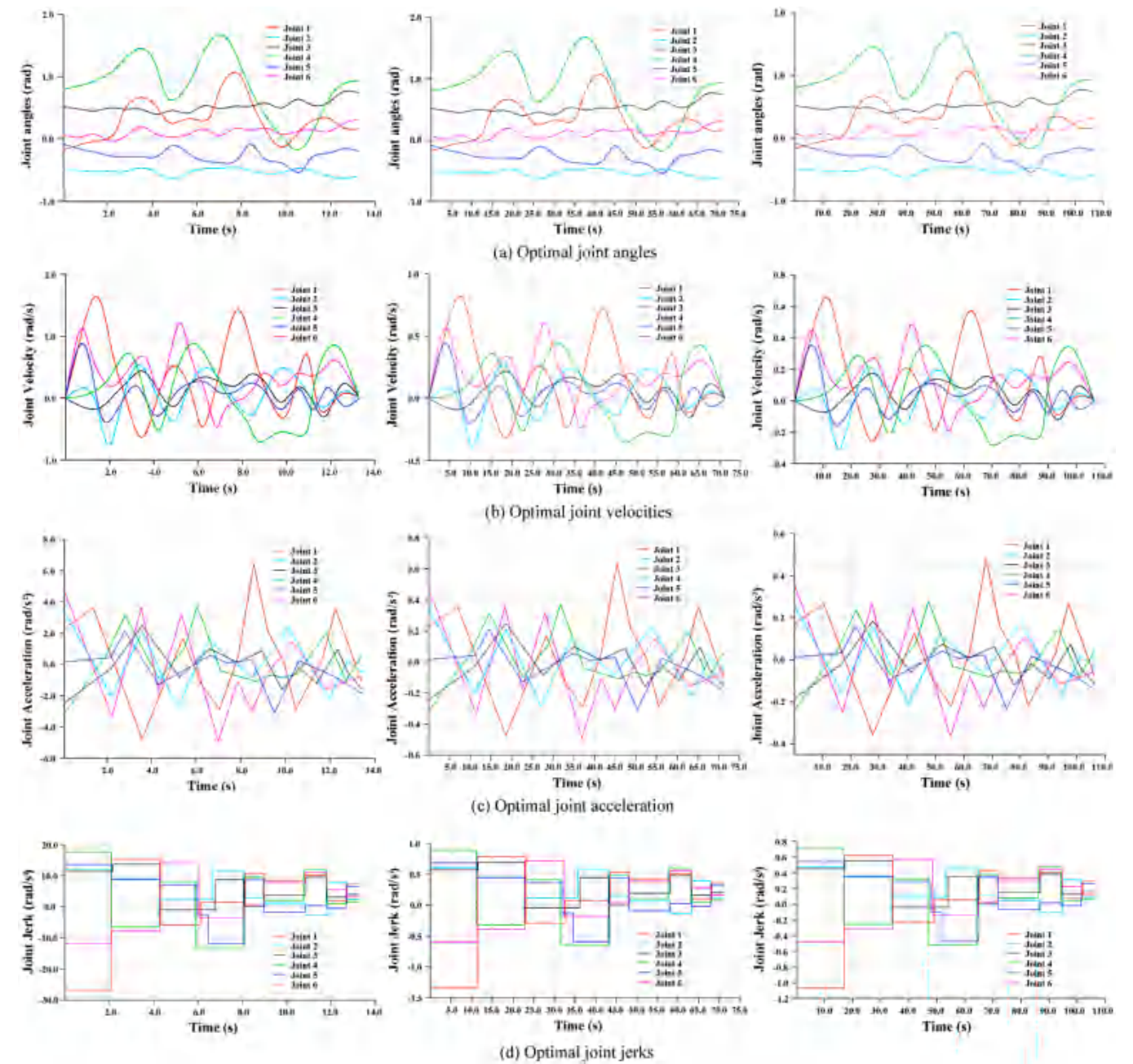


Fig. 16. Optimal results of the cycloid paths (from left to right represent time, impact, and disc wear aspects).

Table 5
Time-impact-disc wear function values of the special solution.

Solutions		Time target value (s)	Jerk target value (mm/s ³)	Disc wear target value (mm)
Time-optimal paths	geodesic	11.53	18.83	0.27
	offset paths			
Jerk-optimal paths	cycloid paths	13.12	28.22	0.66
	geodesic	47.22	0.97	0.16
Disc wear-optimal paths	offset paths			
	cycloid paths	71.94	1.38	0.43
Eclectic optimal paths	geodesic	76.82	0.77	0.08
	offset paths			
Disc wear-optimal paths	cycloid paths	106.74	1.08	0.23
	geodesic	19.31	1.89	0.09
Eclectic optimal paths	offset paths			
	cycloid paths	18.72	2.82	0.18

the problem of obstacles. Although Table 6 gives the ideal data derived from computer graphics, we found some contradictions in the actual grinding work.

The experimental task of this study lasted for several months, running for approximately 15 h a day. The grinding task includes two tasks (upper half and lower half grinding). After the grinding stage, 30° scanning and analysis are carried out, the pump body rotates 30° in the same direction, and grinding and scanning analysis are repeated until the pump body performs 360° grinding as a whole. The grinding work was carried out using an abrasive disc (PFERD, Type: SGP CO-COOL, Dimensions: 180 × 20 × 22.23 mm, produced by PFERD Inc., Germany) with an abrasive grain size equal to 40.

As illustrated in Fig. 22, the grinding work uses the T0 and T1 grinding tool coordinates for grinding the regions of the outlet and bottleneck of the inlet, respectively.

Table 7 lists the grinding parameters used in the actual grinding

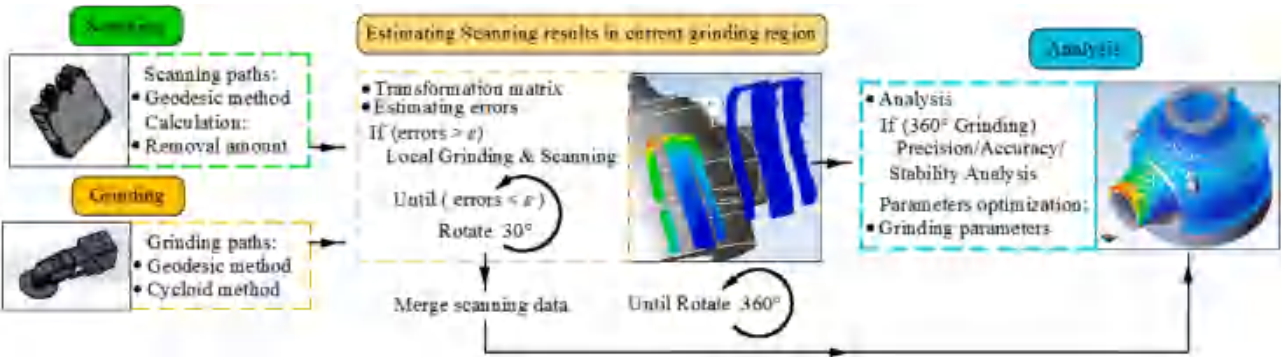


Fig. 17. Schematic diagram of the experimental process.

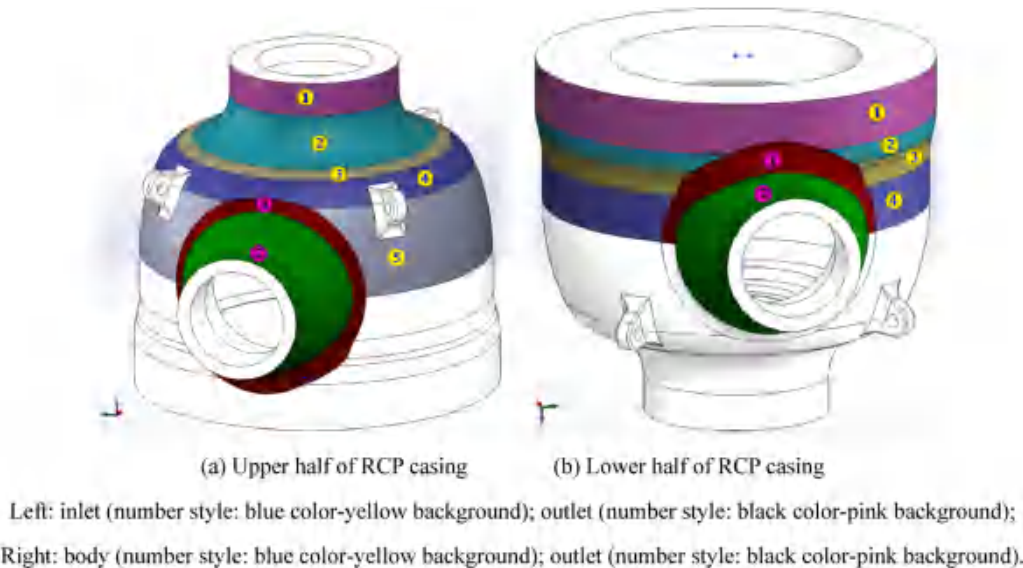


Fig. 18. Processing sequences.

Table 6
Simulation grinding parameters.

Items	Simulation parameters	Upper half				Lower half			
		Inlet		Outlet		Body		Outlet	
Grinding	Inclination angle (°)	①	10	①	10	①	10	①	10
		②	20	②	10	②	10	②	10
		③	15			③	10		
		④	10			④	10		
		⑤	10						
	Chord height (mm)	0.5							
	Path interval (mm)	10							
	Tool coordinate	①	T1/ T2	①	T0	①	T0 & T1/T0 & T2	①	T0
		②	T1/ T2	②	T0	②	T0	②	T0
		③	T1/ T2			③	T0		
		④	T0			④	T0		
		⑤	T0						

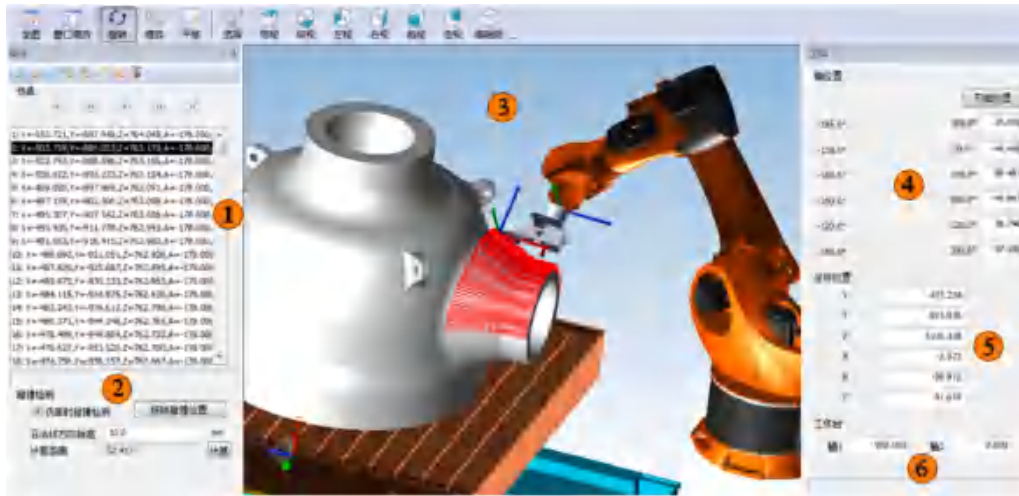


Fig. 19. Grinding simulation.

experiments. Some of the experimental parameters are different from the corresponding simulation parameters in Table 6.

Once the abrasive disc reaches the glazed appearance situation, as illustrated in Fig. 23, the abrasive disc may be replaced.

Fig. 24 and Fig. 25 show the actual grinding procedures and partial grinding effects, respectively.

6.3. Analysis

In this work, the analysis function can evaluate the precision, accuracy, stability, and efficiency of the grinding task. We select 100 regions sampled from 20 casings (i.e., sampling points were selected from 5 regions in each pump casing) and sampled 100 points in each region for further analysis. These 20 RCP casings are equally allocated to four methods for grinding: the manual grinding method, the grinding method without multi-objective optimization, the multi-objective optimization grinding method (using geodesic offset paths), and the multi-objective optimization grinding method (using cycloid paths). Therefore, for each grinding method, samples were taken from 25 regions. The ideal values mentioned below originate from the CAD model.

6.3.1. Precision

After the precision evaluation is performed, the evaluation results can be used to determine whether the difference variation obtained from the repeated test is within the narrow band of different RCP casings.

We perform such a precision evaluation by solving a sample standard deviation problem:

$$s = \sqrt{\frac{\sum_{i=1}^n (\Delta_i - \bar{\Delta})^2}{n-1}} \quad (21)$$

where $n = 100$ is the number of detection points; Δ_i is the minimum distance between the i -th detection point and the design model; and $\bar{\Delta}$ is the average value obtained by summing all the minimum distance values and then dividing by n . The s detected by the four methods are shown in Fig. 26.

For all of the robotization grinding methods, s is small compared with the specified tolerance $\delta = 1.0$ mm (acceptable limits for grinding error of the RCP casing). In addition, all the se deviations, which are obtained by evaluating the s of a sampling distribution, are equal to the ratio of s to the root of n and are less than 0.1 mm (the maximum s is 0.472 mm; therefore, the corresponding se is 9.44×10^{-2} mm), except for the manual grinding method, which means that the robotization grinding results have high precision. The precision of the optimized

paths is better than that of the non-optimized paths, which is presumably because the grinding impact of the optimized path is smaller and the grinding disc wear is also the same. The grinding accuracies of the cycloid paths are slightly better than those of the geodesic offset paths. This is consistent with the fact that the multi-directional path has a certain precision advantage over the one-directional path.

6.3.2. Accuracy

The accuracy is related to the deviation between the 360° scanning data of the RCP casing and the corresponding CAD model. To produce a better contrast result, we compared the final and penultimate grinding effects. After the final region, i.e., the upper half of the outlet, is ground, the maximum 3D deviation does not exceed 0.6 mm, as illustrated in Fig. 27.

After performing repeated measurements as described above, we perform statistics on $\bar{\Delta}$ to verify the accuracy, and the results are listed in Table 8.

The deviations between the grinding results of the optimization methods and the CAD model are superior to those of the grinding results without the optimization method, and the grinding results of all the robotic methods are significantly better than the manual grinding results.

6.3.3. Stability

Stability involves the level of precision and accuracy of the system with respect to time. We employ the Xbar-s control chart to evaluate the stability. It is composed of two charts: the former is used to evaluate the average value with time-variation. The latter is used to evaluate the standard deviation with time-variation. The sampling values are all derived from subgroup values.

To provide frequently updated data and perform a reasonable subgrouping method for the data, we used 10 RCP casings to form a subgroup. The subgroup average \bar{X} of this subgroup can be computed as follows:

$$\bar{X} = \frac{\sum_{i=1}^m X_i}{m} = \frac{X_1 + X_2 + \dots + X_m}{m} \quad (22)$$

where X_1, X_2, \dots, X_n are the individual data (each derived from the average distance between the sampling points and the model) and $m = 10$ is the subgroup size.

Then, we obtain the standard deviation of the i -th subgroup:

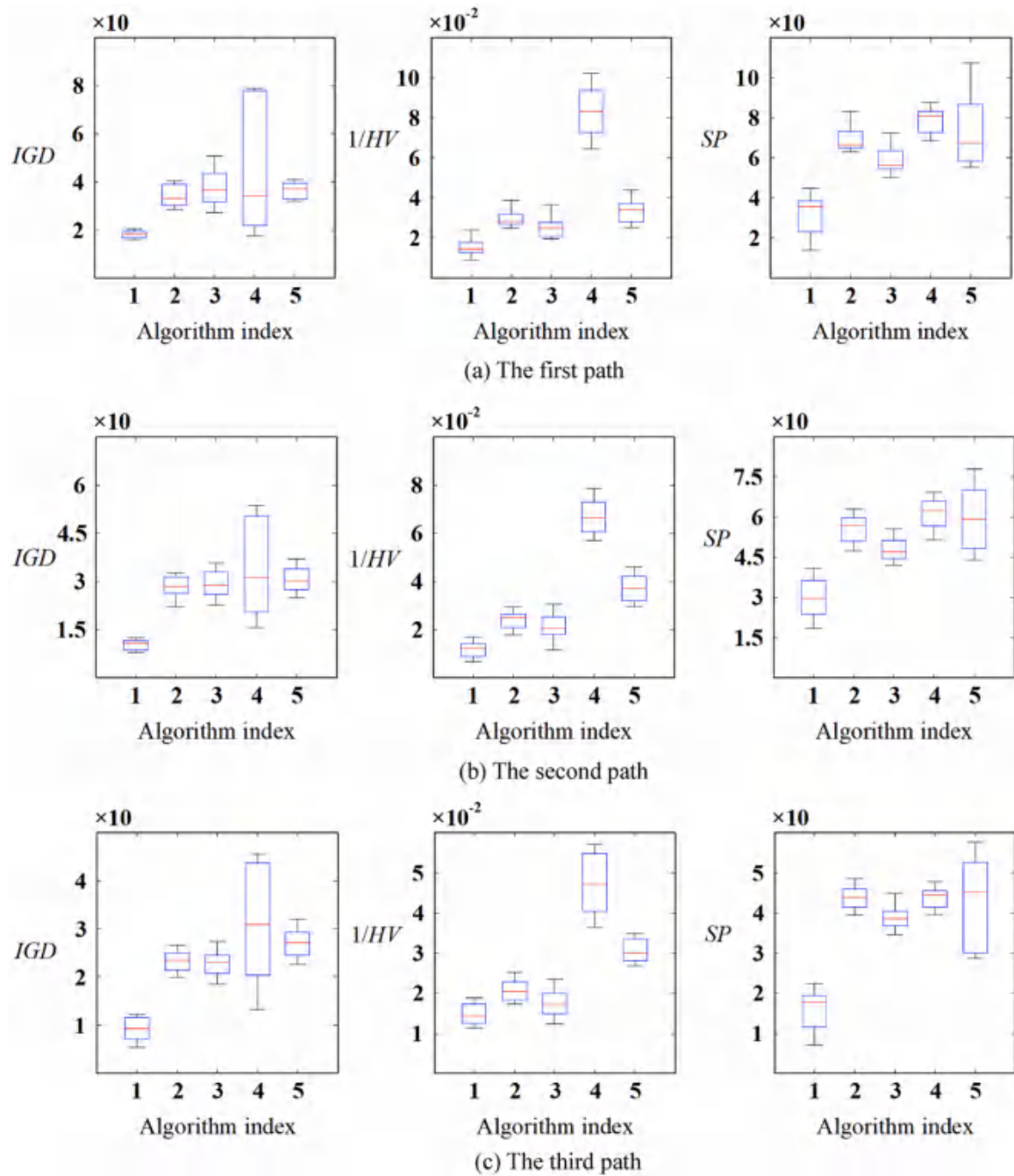


Fig. 20. Indicators of different algorithms on three paths. The numerals on the horizontal axis of each plot indicate the following algorithms: 1: improved NSGA-II, 2: traditional NSGA-II, 3: MOEA/D, 4: OMOPSO, and 5: CMPSO.

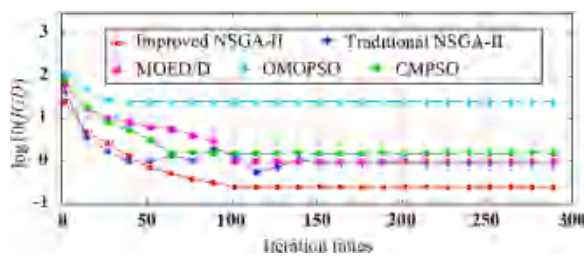


Fig. 21. Convergence curves of the IGD.

$$ss_i = \sqrt{\frac{(X_i - \bar{X})^2}{m-1}} \quad (23)$$

Next, we have the average standard deviation \bar{ss} :

$$\bar{ss} = \frac{\sum_{i=1}^k ss_i}{k} = \frac{ss_1 + ss_2 + \dots + ss_k}{k} \quad (24)$$

where k is the number of subgroups.

Then, the average of the subgroup averages \bar{X} can be calculated:

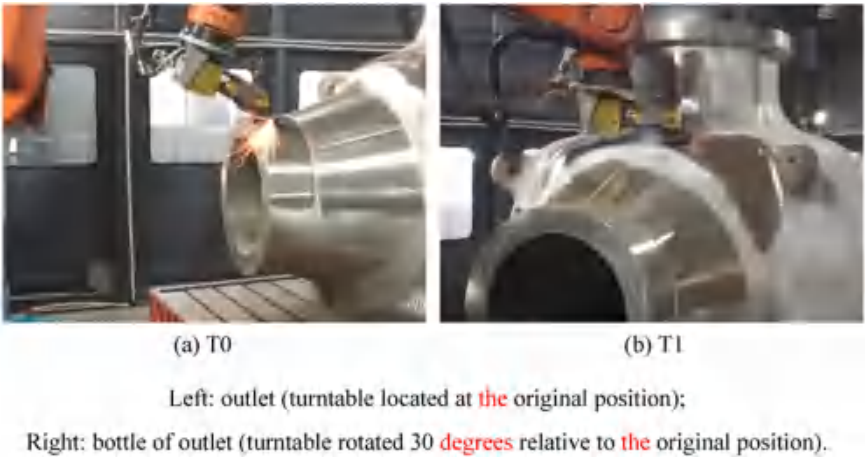


Fig. 22. T0 and T1 grinding tool coordinates.

Table 7
Grinding parameters of the experiment.

Items	Empirical parameters	Upper half				Lower half			
		Inlet		Outlet		Body		Outlet	
Grinding	Inclination angle (°)	①	20	①	10	①	10	①	10
		②	22	②	20	②	10	②	10
		③	15			③	10		
		④	12			④	10		
		⑤	12						
	Chord height (mm)	0.5							
	Path interval (mm)	10							
	Tool coordinate	①	T1/ T2	①	T0	①	T0 & T1/T0 & T2	①	T0
		②	T1/ T2	②	T0	②	T0	②	T0
		③	T1/ T2			③	T0		
		④	T0			④	T0		
		⑤	T0						

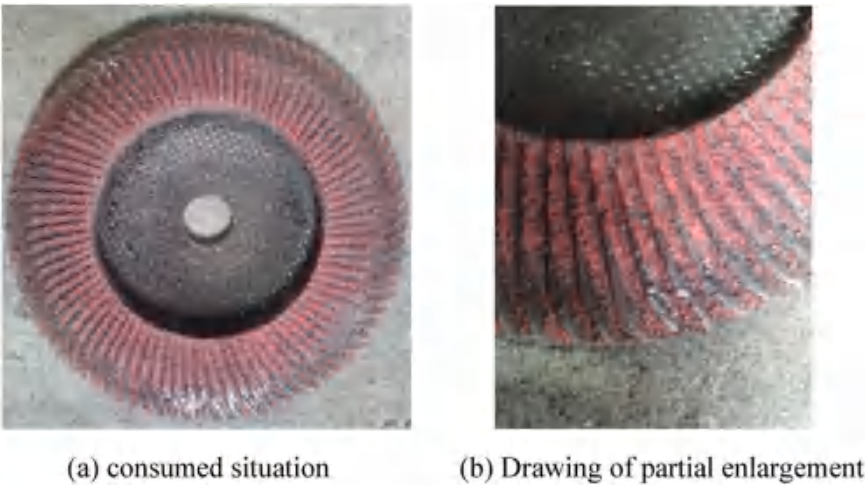


Fig. 23. Glazed appearance of the disc.

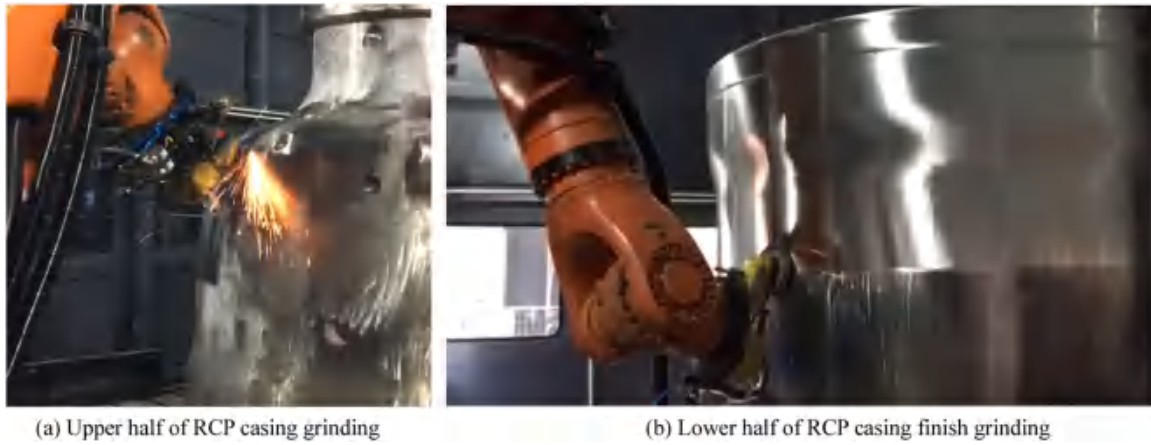


Fig. 24. Grinding procedures.

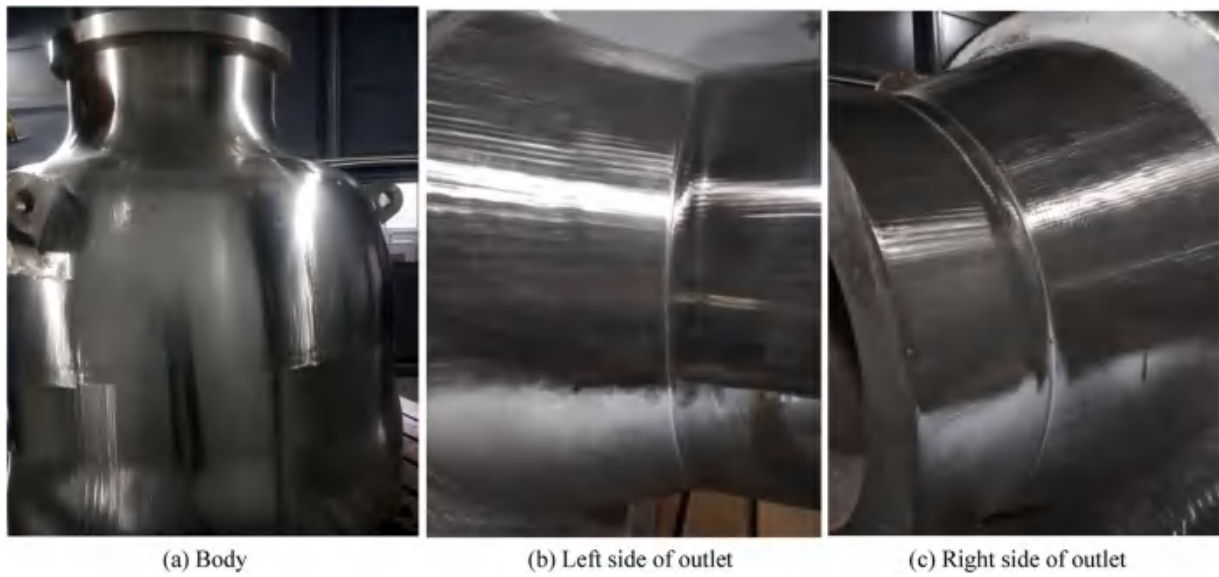


Fig. 25. Grinding effects.

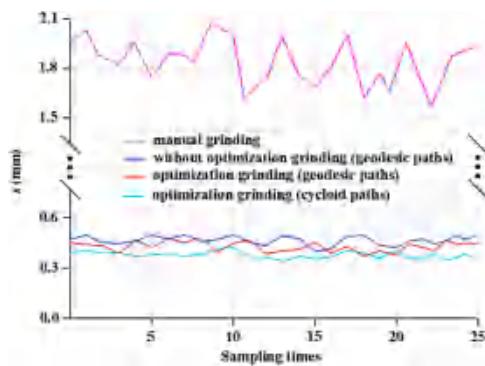


Fig. 26. Precision analysis results of four methods.

$$\bar{\bar{X}} = \frac{\sum_{i=1}^k \bar{X}_i}{k} = \frac{\bar{X}_1 + \bar{X}_2 + \dots + \bar{X}_k}{k} \quad (25)$$

where \bar{X}_k is the average of the observations in the subgroup.

The control bands for the Xbar-s chart then become:

$$\begin{cases} UCL_{\bar{X}} = \bar{\bar{X}} + A_3 \bar{s} \\ LCL_{\bar{X}} = \bar{\bar{X}} - A_3 \bar{s} \\ UCL_{\bar{s}} = B_4 \bar{s} \\ LCL_{\bar{s}} = B_3 \bar{s} \end{cases} \quad (26)$$

where the first two represent the upper and lower control bands of the Xbar chart, respectively; the last two represent the upper and lower control bands of the s chart, respectively; and A_3 , B_4 , and B_3 are control chart constants related to m , and their detailed meanings can be found in

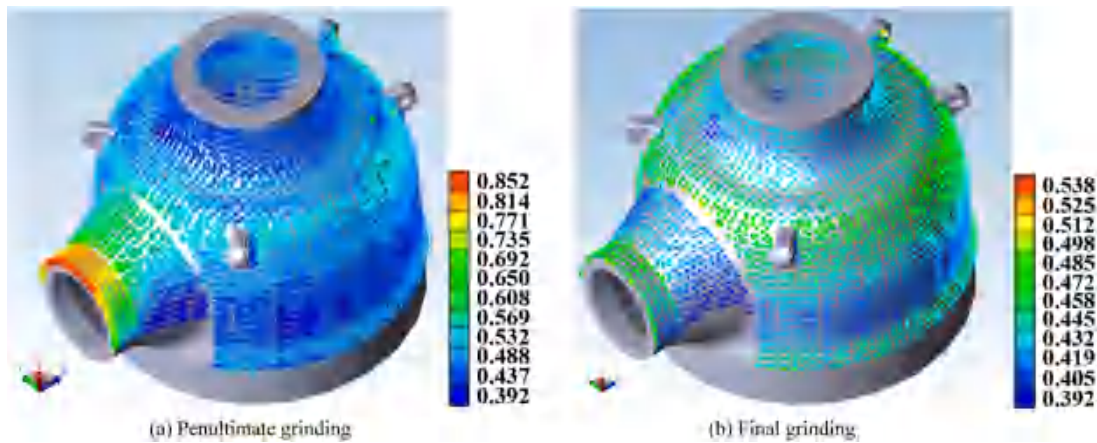


Fig. 27. 3D comparison between two deviations.

Table 8

Accuracy evaluation results of the four grinding methods.

Grinding methods	$\bar{\Delta}$ (mm)
Manual grinding	1.802
Without optimization grinding (geodesic offset paths)	0.237
optimization grinding (geodesic offset paths)	0.223
optimization grinding (cycloid paths)	0.218

reference [58].

We collected data from subgroups every hour for 30 h. The Xbar-s control chart is shown in Fig. 28. Considering that the grinding time consumed by the above four methods is quite different (refer to the related description of the service life of the disc and grinding efficiency below), we provide only a stability evaluation of the optimized grinding (geodesic offset paths) method.

The statistical results are within the control bands and fluctuate randomly on both sides of the centerline: the ordinate values of Xbar fluctuate from 0.227 to 0.273, and the long-term average is close to 0.252, whereas the ordinate values of s fluctuate from 0.422 to 0.472, and the long-term average is close to 0.445. Therefore, the grinding results are stable, consistent and predictable in the near future.

6.3.4. Service life of the disc and grinding efficiency

Manual grinding consumes the grinding disc faster, and the service life of the grinding disc is generally 10 h. After robotic grinding without multi-objective optimization is implemented, the service life of the grinding disc is approximately 6 h. Moreover, the service life of the grinding disc can reach 50 h after optimized geodesic offset paths with the same processing parameters are implemented. However, the other conditions are the same, and the optimized cycloid path can provide a service life of only nearly 10 h. The multi-directional paths produce varying grinding contact forces and varying disc sliding velocities, which lead to more complex material removal depths, thus affecting the

service life of the grinding disc.

We compared the grinding efficiency of these four methods. The manual grinding method consumed approximately 40 h by two experienced workers (during this period, approximately 8 to 9 grinding discs were consumed). The robotization grinding method (without multi-objective optimization) requires 25 h to achieve the grinding task (during this period, approximately 4 to 5 grinding discs are consumed, and tool coordinate system calibration needs to be performed again every time the grinding disc is replaced). The cycloid grinding method takes 30 h to achieve the grinding task (during this period, approximately 3 to 4 grinding discs are consumed, and it is also necessary to consider the time consumption of the tool coordinate system recalibration). However, the geodesic offset paths take 15 h to achieve the grinding task. Therefore, it is the most suitable method for grinding RCP casings among these methods.

7. Conclusions

The inherent vibration of any flexible mechanism, e.g., a 6-axis manipulator, may limit the grinding quality and productivity, and the consumption of grinding discs increases the complexity of this problem. For heavy-duty robots that grinding RCP casings, it is a great challenge for robots to realize smooth, efficient, and continuous disc grinding (less disc replacement), let alone to efficiently remove a relatively large volume of materials.

In this paper, a path planning method based on an improved NSGA-II algorithm to solve the optimization problem of the grinding time, impact, and disc wear is presented for performing disc grinding on an RCP casing. Our method has the following advantages:

1. A grinding disc wear model suitable for rigid grinding tasks is proposed, and its effectiveness is verified through the finite element and experimental methods. It can accurately predict the wear conditions of grinding discs during the grinding process;
2. By calculating linear geodesic offset paths and converting them to NURBS interpolation paths, the stable and continuous grinding motion

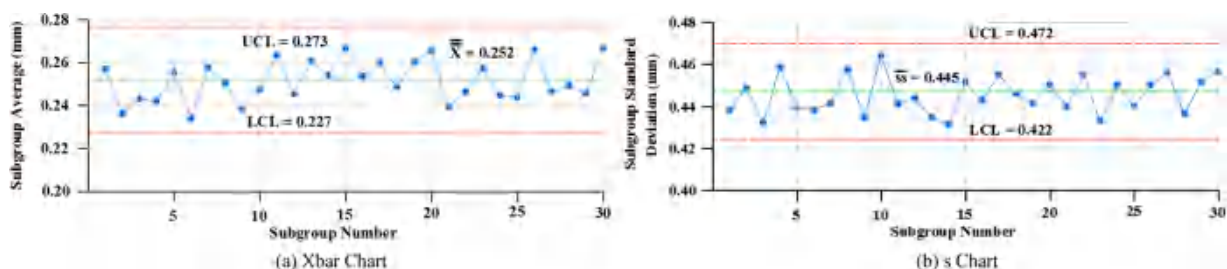


Fig. 28. Xbar-s control chart.

can be guaranteed;

3. The S-shaped ACC/DEC feedrate planning results can be converted to the corresponding angular velocity, acceleration, and jerk of each joint in joint space, ensuring that the robot performs grinding tasks under appropriate kinematic constraints;

4. An improved NSGA-II algorithm is proposed, and its performance is validated in three indicators on a benchmark test problem suite. The results show that the proposed algorithm can achieve the desirable solution in most benchmark problems;

5. Establish the optimization function and incorporate it with kinematic constraints into the improved NSGA-II algorithm to solve the compromise minimization problem of traveling time, actuator jerk, and disc wear; The excellent performance of the proposed algorithm in terms of efficiency and convergence was validated for the grinding paths;

6. The experimental results show that from the perspective of the service life and grinding efficiency of the disc, our method possesses high grinding efficiency while ensuring the service life of the grinding disc. Stability tests show that the grinding results are stable and predictable.

In future research, we plan to improve the grinding disc wear model to optimize the objective function by collecting data on glazed appearance formation under different grinding conditions. In addition, we plan to use more advanced grinding devices to verify the applicability of the proposed method and the effectiveness of improving the grinding accuracy.

Ethical Approval

Not applicable.

Consent to Participate

Not applicable.

Consent to Publish

Not applicable.

Funding

This research is supported by the National Natural Science Foundation of China (grant no. 51605475), the Liaoning Provincial Science and Technology Plan Project (grant no. 2022-MS-040), and the Central Guidance for Local Scientific and Technological Development Funds (grant no. 2021JH6/10500123).

CRedit authorship contribution statement

Bo Zhou: Writing – review & editing, Writing – original draft, Visualization, Validation, Software, Funding acquisition, Formal analysis. **Tongtong Tian:** Visualization, Validation, Software.

Declaration of Competing Interest

The authors declare that they have no competing interests.

Acknowledgments

The authors are grateful for the support provided by the National Natural Science Foundation of China (grant no. 51605475), the Liaoning Provincial Science and Technology Plan Project (grant no. 2022-MS-040), and the Central Guidance for Local Scientific and Technological Development Funds (grant no. 2021JH6/10500123).

Availability of data and materials

All data generated or analyzed during this study are included in this published article.

References

- [1] Xiao MB, Ding Y, Fang Z, Yang G. Contact force modeling and analysis for robotic tilted-disc polishing of freeform workpieces. *Precis Eng* 2020;66:188–200.
- [2] Pandiyan V, Murugan P, Tjahjowidodo T, Caesarendra W, Manyar OM, Then DJH. In-process virtual verification of weld seam removal in robotic abrasive belt grinding process using deep learning. *Robot Comput-Integr Manuf* 2019;57:477–87.
- [3] Masanori A. Imaging diagnosis of classical and new pneumoconiosis: predominant reticular HRCT pattern. *Insights Imaging* 2021;12(1):1–9.
- [4] Zhu DH, Feng XZ, Xu XH, Yang ZY. Robotic grinding of complex components: A step towards efficient and intelligent machining – challenges, solutions, and applications. *Robot Comput-Integr Manuf* 2020;65:101908.
- [5] Tao B, Zhao X, Ding H. Mobile-robotic machining for large complex components: a review study. *Sci China Technol Sci* 2019;62(8):1388–400.
- [6] Yuan L, Pan Z, Ding D, Sun S, Li WM. A review on chatter in robotic machining process regarding both regenerative and mode coupling mechanism. *IEEE/ASME Trans Mechatron: A Jt Publ IEEE Ind Electron Soc ASME Dyn Syst Control Div* 2018;23(5):2240–51.
- [7] Wang C, Wu YR, Liao HZ, Deng C, Luo J, Huang Y. Influence of contact force and rubber wheel hardness on material removal in abrasive belt grinding investigated by physical simulator. *Precis Eng* 2022;78:70–8.
- [8] Yan SJ, Xu XH, Yang ZY, Zhu DH. An improved robotic abrasive belt grinding force model considering the effects of cut-in and cut-off. *J Manuf Process* 2019;37:496–508.
- [9] Pandiyan V, Caesarendra W, Tjahjowidodo T, Tan HH. In-process tool condition monitoring in compliant abrasive belt grinding process using support vector machine and genetic algorithm. *J Manuf Process* 2018;31:199–213.
- [10] Mezghani S, Mansori ME, Sura E. Wear mechanism maps for the belt finishing of steel and cast iron. *Wear* 2009;267(1):86–91.
- [11] Nasri H, Bolmsjo G. A process model for robotic disc grinding. *Int J Mach Tools Manuf* 1995;35(4):503–10.
- [12] Ulrich BJ, Srivastava AK, Elbestawi MA. Analysis of the robotic disc grinding process. *Int J Adv Manuf Technol* 1992;7:82–92.
- [13] Wang C, Wu YR, Liao HZ, Deng C, Luo J, Huang Y. Influence of contact force and rubber wheel hardness on material removal in abrasive belt grinding investigated by physical simulator. *Precis Eng* 2022;78:70–8.
- [14] Lu A, Jin T, Guo ZF, Qu MN, Chang YP, Liu QF, Zhang C. Characterization of the tool influence function in a dual-axis wheel polishing process to achieve high material removal rates. *Precis Eng* 2018;52:276–90.
- [15] Zhou B, Tian TT, Zhu G, Zhao JB, Liu DH. An Ultrasonic Testing Method for Wall Thickness of Turbine Blades. *Measurement* 2022;198:111357.
- [16] Ma W, Hu TL, Zhang CR, Zhang TJ. A robot motion position and posture control method for freeform surface laser treatment based on NURBS interpolation. *Robot Comput-Integr Manuf* 2023;83:102547.
- [17] Song DD, Xue F, Wu DD, Zhang J, Zhang X, Zhao WH, Lu BH. Iso-parametric path-planning method of twin-tool milling for turbine blades. *Int J Adv Manuf Technol* 2018;98:3179–89.
- [18] Yuan CM, Mi ZP, Jia XH, Lin FM, Shen LY. Tool orientation optimization and path planning for 5-axis machining. *J Syst Sci Complex* 2021;34:83–106.
- [19] Shahzadeh A, Khosravi A, Robinette T, Nahavandi S. Smooth path planning using biclothoid fillets for high speed CNC machines. *Int J Mach Tools Manuf* 2018;132:36–49.
- [20] Hauth S, Linsen L. Cycloids for polishing along double-spiral toolpaths in configuration space. *Int J Adv Manuf Technol* 2012;60:343–56.
- [21] Tagliavini A, Bianco CGL. η 3D-splines for the generation of 3D Cartesian paths with third order geometric continuity. *Robot Comput-Integr Manuf* 2021;72:102203.
- [22] Lu YA, Tang K, Wang CY. Collision-free and smooth joint motion planning for six-axis industrial robots by redundancy optimization. *Robot Comput-Integr Manuf* 2021;68:102091.
- [23] Huang T, Zhao D, Cao ZC. Trajectory planning of optical polishing based on optimized implementation of dwell time. *Precis Eng* 2020;62:223–31.
- [24] Li XF, Zhao H, He XM, Ding H. A novel cartesian trajectory planning method by using triple NURBS curves for industrial robots. *Robot Comput-Integr Manuf* 2023;83:102576.
- [25] Xu J, Yang H, Liu M, Tian J, Liu B. Research on winding trajectory planning for elbow pipe based on industrial robot. *Int J Adv Manuf Technol* 2017;93(1–4):537–45.
- [26] Ma W, Hu TL, Zhang CR, Zhang TJ. A robot motion position and posture control method for freeform surface laser treatment based on NURBS interpolation. *Robot Comput Manuf* 2023;83:102547.
- [27] Gao LD, Lv WY, Yan XY, Han YZ. Complete coverage path planning algorithm based on energy compensation and obstacle vectorization. *Expert Syst Appl* 2022;203:117495.
- [28] Kim J, Kim SR, Kim SJ, Kim DH. A practical approach for minimum-time trajectory planning for industrial robots. *Ind Robot* 2010;37(1):51–61.
- [29] Dong H, Zhong XF, Huang S. Trajectory planning method in joint space for 6-DOF robot. *J Zhejiang Univ Technol* 2015;43(3):336–9.

- [30] Wang XK, Li G, Zhou DK, Yang ZY. Time-Optimal trajectory planning algorithm based on DE for manipulator. *Comput Simul* 2015;32(8):332–7.
- [31] Soori M, Arezoo B, Dastres R. Optimization of Energy Consumption in Industrial Robots, A Review. *Cogn Robot* 2023;3(1):142–57.
- [32] Zhou J, Yi H, Cao HJ, Jiang P, Zhang CY, Ge WW. Structural decomposition-based energy consumption modeling of robot laser processing systems and energy-efficient analysis. *Robot Comput-Integr Manuf* 2022;76:102327.
- [33] Gasparetto A, Zanotto V. A technique for time-jerk optimal planning of robot trajectories. *Robot Comput-Integr Manuf* 2008;24(3):415–26.
- [34] Piazzzi A, Visioli A. Global minimum-jerk trajectory planning of robot manipulators. *IEEE Trans Ind Electron* 2000;47(1):140–9.
- [35] Xu HL, Xie XR, Zuang J, Wang SA. Global time-energy optimal planning of industrial robot trajectories. *J Mech Eng* 2010;46(09):19–25.
- [36] Cao ZY, Wang H, Wu WR, Xie HJ. Time-jerk optimal trajectory planning of shotcrete manipulators. *J Cent South Univ (Sci Technol)* 2013;44(1):114–21.
- [37] Weng LG, Wang A, Xia W, Ji ZZ. Research on mobile robot path planning based on improved SPEA2 Algorithm. *Comput Simul* 2015;31(7):346–50.
- [38] Cheng YL, Zhu SQ, Liu SG. Inverse kinematics of 6R robots based on the orthogonal character of rotation sub-matrix. *Robot* 2008;30(2):160–4.
- [39] Wang ZL, Chen WD. Robot workcell layout optimization based on joint space evaluation. *J Shanghai Jiaotong Univ* 2009;43(11):1762–6.
- [40] Huang J, Hu P, Wu K, Zeng M. Optimal time-jerk trajectory planning for industrial robots. *Mech Mach Theory* 2018;121:530–44.
- [41] Bureerat S, Pholdee N, Radpukdee T, Jaroenapibal P. Self-adaptive MRPBIL-DE for 6D robot multiobjective trajectory planning. *Expert Syst Appl* 2019;136:133–44.
- [42] Whitney DE, Edsall AC, Todtenkopf AB, Kurfess TR, Tate AR. Development and Control of an Automated Robotic Weld Bead Grinding System. *J Dyn Syst Meas Control* 1990;112(2):166–76.
- [43] Biswas A, Deekshatulu BL, Roy SS. Energy Optimal Trajectory Planning of a Robotic Manipulator Using Genetic Algorithm. *Am Inst Phys* 2010;1298(1):492–7.
- [44] Xin SQ, Ying X, He Y. Efficiently computing geodesic offsets on triangle meshes by the extended Xin–Wang algorithm. *Comput-Aided Des* 2011;43(11):1468–76.
- [45] Kazhdan M, Hoppe H. Screened poisson surface reconstruction. *Acm Trans Graph* 2013;32(3):1–13.
- [46] Kobbelt Bommes D. Accurate computation of geodesic distance fields for polygonal curves on triangle meshes. : *Proc Vis, Model, Vis Conf* 2007:151–60.
- [47] Li JX, Zhou B, Li L, Zhao JB, Zhu G, Cai M. A method for analyzing the texture features of free-form surface polishing paths based on co-occurrence matrix 2023; 124(1–2):601–18.
- [48] Wardetzky M, Bergou M, Harmon D, Zorin D, Grinspun E. Discrete quadratic curvature energies. *Comput Aided Geom Des* 2007;24(8–9):499–518.
- [49] Zhou B, Zhao JB, Li L, Xia RB. NURBS curve interpolation algorithm based on tool radius compensation method. *Int J Prod Res* 2016;54(15):4448–74.
- [50] Verma S, Pant M, Snasel V. A Comprehensive Review on NSGA-II for Multi-Objective Combinatorial Optimization Problems. *IEEE Access* 2021;9:57757–91.
- [51] Deb K, Pratap A, Agarwal S, et al. A fast and elitist multiobjective genetic algorithm: NSGA-II. *IEEE Trans. Evolut Comput* 2002;6(2):182–97.
- [52] Liu Y, Tang Q, Tian XC, Yang S. A novel offline programming approach of robot welding for multi-pipe intersection structures based on NSGA-II and measured 3D point-clouds. *Robot Comput-Integr Manuf* 2023;83(14):102549.
- [53] Deb K, Deb D. Analysing mutation schemes for real-parameter genetic algorithms. *Int J Artif Intell Soft Comput* 2014;4(1):1–28.
- [54] Hu ZY, Yang JM, Cui HH, Sun H, Wei LX. Multi-objective particle swarm optimization algorithm based on leader combination of decomposition and dominance 2017;33(3):1577–88.
- [55] Coello CC, Pulido GT. Multiobjective structural optimization using a microgenetic algorithm. *Struct Multidiscip Optim* 2005;30(5):388–403.
- [56] Zitzler E, Thiele L. Multi-objective evolutionary algorithms: a comparative case study and the strength Pareto approach. *IEEE Trans Evolut Comput* 1999;3(4):257–71.
- [57] Bandyopadhyay S, Pal SK, Aruna B. Multi-objective Gas, quantitative indices, and pattern classification. *IEEE Trans Syst, Man, Cybern, Part B(Cybern)* 2004;34(5):2088–99.
- [58] Lorenzen TJ, Vance LC. The economic design of control charts: A unified approach. *Technometrics* 1986;28:3–10.